The effects of heat treatment on the response of WE43 Mg alloy: crystal plasticity finite element simulation and SEM-DIC experiment

Sriram Ganesan [a], Mohammadreza Yaghoobi [b],[*], Alan Githens [b], Zhe Chen [c], Samantha Daly [c], John E. Allison [b], Veera Sundararaghavan [a]

[a] Aerospace Engineering, University of Michigan, Ann Arbor, MI, 48109, USA
[b] Materials Science and Engineering, University of Michigan, Ann Arbor, MI, 48109, USA
[c] Mechanical Engineering, University of California at Santa Barbara, Santa Barbara, CA, 93106, USA

A B S T R A C T

The present work addressed the effects of heat treatment on the mechanical response of a WE43 Mg alloy using an integrated framework of SEM-DIC experiment and CPFE simulation. Both macroscopic responses including yield strength, ultimate strength, ductility, and microscopic responses, including local displacement and strain maps, were experimentally investigated. The focus of this work is to use the CPFE simulation as an integrated computational tool to study the effects of heat treatment. The CPFE framework was evaluated using the local fields of displacement and strain obtained from the SEM-DIC experiment rather than the conventional scheme of using macroscopic responses at different loading directions. Subsequently, the information which is available using CPFE, such as the critical resolved shear stress (CRSS) and relative slip activity, was used to study the effects of heat treatment on the response of WE43 Mg alloy. The contributions of different strengthening mechanisms on the CRSS were addressed. The results show that effects of heat treatment can be captured using the predominant mechanisms of the grain size effect and the influence of precipitates. Finally, it has been shown that classical Hall-Petch in which one constant can capture the size effects, should be modified. To do so, each deformation mode should have a unique Hall-Petch constant, which are calculated here for the WE43 Mg alloy.

1. Introduction

Slip and extension twinning are the dominant deformation mechanisms in Mg alloys (Begum et al., 2009; Beyerlein et al., 2010; Mirza et al., 2013; Mokdad and Chen, 2015; Yu et al., 2015; Murphy-Leonard et al., 2019; Yaghoobi et al., 2020). Depending on the material microstructure and applied loading, slip mechanisms of basal $< a >$, prismatic $< a >$, pyramidal $< a >$, and pyramidal $< c + a >$, along with one extension twin mode ($\{10\overline{1}2\}\overline{1}011$) govern plasticity in Mg alloys. The most active slip mode in Mg and its alloys is generally basal $< a >$, as it has the lowest critical resolved shear stress (CRSS). However, this is not always the case. For example, basal slip does not activate during tensile deformation along the c-axis; instead, extension twinning becomes the governing deformation

---

* Corresponding author.
  E-mail address: yaghoobi@umich.edu (M. Yaghoobi).

mechanism in Mg alloys (Knezevic et al., 2010; Wu et al., 2010; Murphy-Leonard et al., 2019; Yaghoobi et al., 2019, 2020). In the case of pure tension along the c-axis, the resolved shear stresses of basal $< a >$, prismatic $< a >$, and pyramidal $< a >$ are zero, and these slip modes are not activated. The CRSS of pyramidal $< c + a >$ is commonly much larger than that of the extension twinning. Consequently, in the case of tension along c-axis the extension twinning becomes the dominant deformation mechanism. In the case of deformation which is not exactly along $<a>$ or $<c>$ axis, all the slip systems can potentially be activated and their contributions depend on the deformation gradient and relative CRSS of the slip systems. Similarly, extension twinning dominates in wrought Mg alloys during compression loading parallel to the basal plane, which leads to the $86.3°$ reorientation of the basal pole. This complexity in deformation modes of Mg and its alloys leads to a highly anisotropic response. The effects of microstructure on twinning and the micromechanics of twinning have been widely studied by different researchers (Capolungo and Beyerlein, 2008; Wang et al., 2009; Beyerlein et al., 2010, 2011; Beyerlein and Tomé, 2010; Zheng et al., 2012; Barrett and El Kadiri, 2014; Beyerlein and Arul Kumar, 2018). The twin nucleation and growth in Mg alloys are governed by various factors, such as the nominal Schmid Factor and characteristics of the neighboring grains.

Crystal plasticity is widely used to investigate deformation mechanisms in Mg alloys, including slip and twinning (Van Houtte, 1978; Tomé et al., 1991; Kalidindi, 1998; Staroselsky and Anand, 2003; Abdolvand et al., 2011, 2015; Fernández et al., 2011, 2013; Zhang and Joshi, 2012; Oppedal et al., 2012, 2013; Wang et al., 2013a, 2013b; Liu and Wei, 2014; Ardeljan et al., 2015; Kabirian et al., 2015; Qiao et al., 2015, 2016; Lévesque et al., 2016; Hama et al., 2016, 2017; Prasad et al., 2017; Feather et al., 2019). These models have successfully captured the anisotropic response of Mg alloys under various loading conditions. However, models have been largely verified using the macroscopic stress-strain behavior and have not been generally compared against the microscale details of plastic deformation occurring in the sample. One important drawback of this macroscale comparison is that different, non-unique combinations of material inputs may capture the same stress-strain response. Thus, the governing deformation mechanisms cannot necessarily be uniquely identified by these comparisons of macroscale experimental results and CPFE simulations. Recently, different experimental frameworks, including x-ray diffraction and microscale digital image correlation, have been developed to further verify crystal plasticity simulations. Synchrotron X-ray techniques, such as three-dimensional X-ray diffraction (3DXRD) or high-energy diffraction microscopy (HEDM), also provide a means to further verify crystal plasticity simulations (Shade et al., 2019). HEDM provides *in-situ* measurements of strain and stress for each grain during deformation (Greeley et al., 2019). In addition, the 3D microstructure of the sample can be obtained using HEDM for use in the crystal plasticity simulation. These techniques have been successfully used to capture the governing deformation mechanisms in Mg alloys. Abdolvand et al. (2015) combined synchrotron X-ray diffraction experiments with crystal plasticity finite element (CPFE) simulation to study deformation twinning in an AZ31B Mg alloy. Lentz et al. (2015) conducted *in-situ* X-ray synchrotron diffraction experiments and elasto-plastic self-consistent modeling to study the effect of age hardening on the deformation behavior of a WE54 Mg alloy. Wang et al. (2018) investigated the deformation mechanisms of Mg–Y alloy by using viscoplastic self-consistent (VPSC) modeling with HEDM. Greeley et al. (2019) incorporated the HEDM with CPFE to investigate the evolution of deformation in an Mg–Nd alloy. Digital Image Correlation (DIC) is another technique that can be used to further validate crystal plasticity simulations. Martin et al. (2014) investigated the deformation mechanisms of a ZEK100 Mg alloy using DIC along with the full-field viscoplastic Fast Fourier Transform (VPFFT) crystal plasticity simulation, and Githens et al. (2020) investigated the micromechanics of WE43-T5 Mg alloy using a coupled CPFE and DIC framework.

Several experimental studies have investigated the effects of heat treatment on WE43 Mg. Two common heat treatments of WE43 Mg alloys are T5 and T6 conditions. The hot rolled and aged WE43 sample is commonly called WE43-T5. This condition does not incorporate a specific solution treatment step between the rolling and aging steps. The T5 condition can be solution treated and subjected to another aging treatment which leads to the WE43-T6 sample. Yu et al. (2008) investigated the microstructure and mechanical properties of hot-rolled WE43-T5 and WE43-T6 and reported that these conditions can reach higher hardness and strength compared to as-cast samples. Furthermore, in this study, the T5 condition shows improved mechanical properties compared to the T6 condition, while in the T6 condition strengthening precipitates produced by aging were larger than those of the T5 condition. Adams et al. (2016) studied the very high cycle fatigue behavior of Mg alloys WE43-T5 and WE43-T6. They investigated the role of crack initiation and short crack growth on fatigue life in the very high cycle fatigue regime using the ultrasonic axial fatigue tests. Adams et al. (2016) reported that in their investigation the T5 condition had finer grains and higher fatigue strength compared to a T6 heat treatment. Furthermore, they showed that the average short crack growth rate is similar for T5 and T6 conditions. Also, in both heat treatment conditions, the underlying mechanism of crack initiation is the cyclic slip deformation in particularly large and favorably oriented grains. Bhattacharyya et al. (2017) studied the effects of different heat treatments of T5 and T6 on the mechanical properties of WE43 Mg alloy. They also reported that the size and volume fraction of precipitates in this T6 condition is slightly larger than that observed in a T5 condition. However, the yield strength of the T6 condition was considerably lower than T5, which can be attributed to a larger grain size of T6. Xiang et al. (2018) addressed the effect of heat treatment on the mechanical and microstructural properties of WE43 Mg alloy. Accordingly, as-cast and T5 conditions were compared. The results showed that the mean grain size reduced from 54.1 μm in the as-cast condition to 24.8 μm in a T5 condition. The tensile yield strength, average tensile ultimate strength, Young's modulus, compressive yield strength, and average compressive ultimate strength are enhanced by 40%, 53%, 16%, 55%, and 23%, respectively, in the T5 condition compared to as-cast condition. The crack initiation mechanism of WE43 also changes from initiation at the eutectic region located at the grain boundaries in the as-cast sample to the grain boundary sliding in WE43-T5 samples. Jahedi et al. (2018) and Ghorbanpour et al. (2019) also investigated heat treatment effects on the mechanical properties of WE43 Mg, including the deformation behavior, uniaxial and cyclic response, and fatigue life.

In order to elaborate on the underlying deformation mechanisms that are affected by these heat treatment changes, it is helpful to use an integrated framework, including both experiment and simulation. Towards this end, an integrated framework (Aagesen et al., 2018) for experiments and multi-scale simulations has been developed to link the microstructural features of metals and alloys with

predictions of their mechanical behavior. An open-source, massively parallel 3-D crystal plasticity finite element (CPFE) software package PRISMS-Plasticity (Yaghoobi et al., 2019) plays a key role in this integrated framework. In the case of Mg and its alloys, both slip and twinning mechanisms are incorporated in the PRISMS-Plasticity CPFE software to accurately capture the deformation mechanisms.

In this work, an integrated framework, including digital image correlation under scanning electron microscopy (SEM-DIC) and
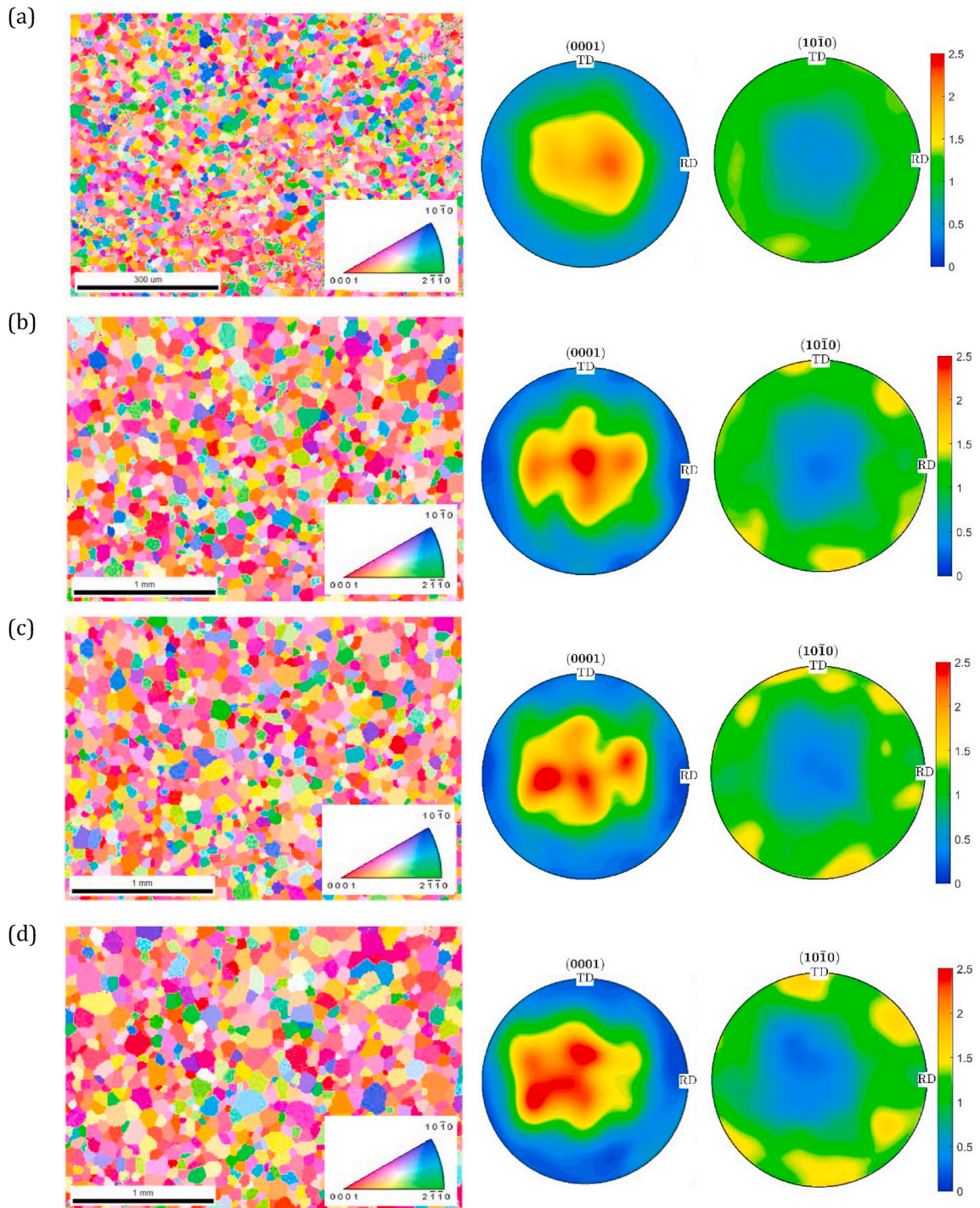

Fig. 1. Inverse pole figure (IPF) maps and texture plots of (a) as-received T5 condition (b) solution treated (ST) condition (c) ST+4 h aged and (d) ST+16 h aged (T6 condition).

CPFE simulation is used to investigate the effects of heat treatment on the response of Mg WE-43. First, the effects of various heat treatments on both macro- and micro-mechanical properties, including yield strength, ultimate strength, full-field strains, and probability distributions of strain, are experimentally investigated. Electron backscatter diffraction (EBSD), custom nanoparticle patterning processes for corrosion-susceptible alloys (Githens and Daly, 2017), scanning electron microscopy (SEM), in-SEM uniaxial tensile loading, and digital image correlation (DIC) were combined to obtain full-field strain maps on the length scale of the microstructure and their relation to the sample texture. The open-source CPFE software, PRISMS-Plasticity, was used to capture the response, including slip and twinning, of the WE43-T6 Mg alloy sample (Yaghoobi et al., 2019). The representative volume element (RVE) for the polycrystal was generated using the open-source software Neper (Quey et al., 2011), and the accuracy and convergence of the texture were investigated. CPFE parameters were calibrated using the stress-strain response of the WE43-T6 sample during uniaxial compression and tension from the generated RVE, and the slip and twin activity were analyzed. In the next step, the full-field strain map of WE43-T6, obtained from SEM-DIC experiment, was compared with the CPFE simulation results. Accordingly, the local distribution of strain, slip, and twin activity was studied. Finally, both CPFE simulation and SEM-DIC results of the T6 condition were compared to those of the T5 condition, which were reported by Githens et al. (2020), to examine the governing mechanisms of heat treatment effects.

2. Material and experimental methods

The as-received WE43-T5 was in the form of a hot-rolled and aged plate, which had an average grain size of 12 μm as measured using EBSD (Githens et al., 2020). Samples were then solution treated in an open-air furnace at 525°C for 8 h, followed by a water quench (ST condition). The average grain size of the solution treated material was 122 μm. The material underwent considerable grain
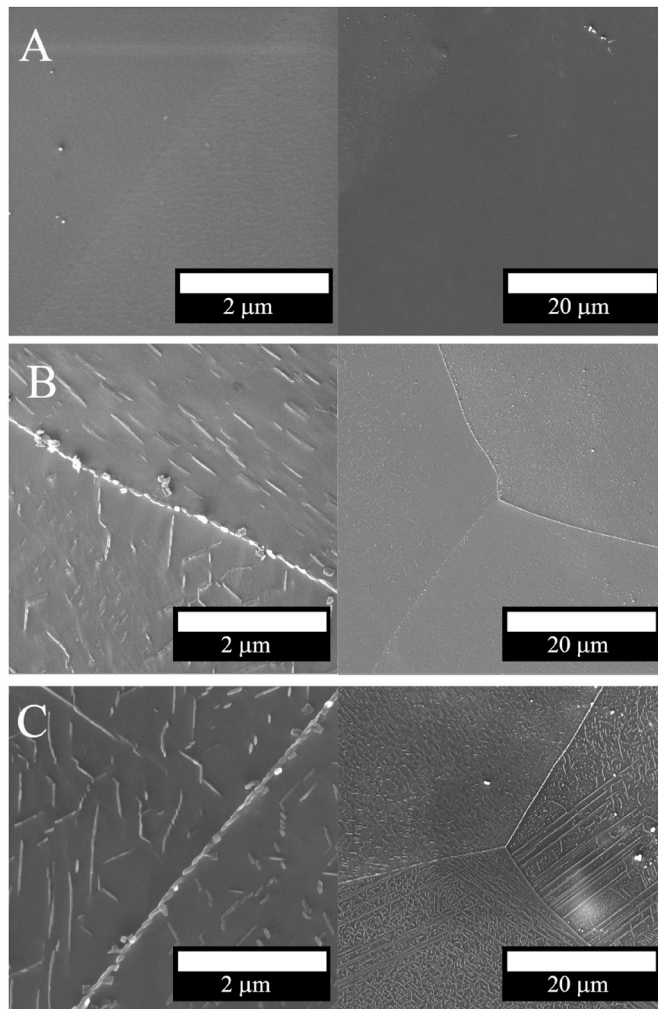

Fig. 2. SEM images of precipitate structures on (a) solution treated (ST) condition (b) ST+4 h aged (c) ST+16 h aged (T6 conditions). Precipitates nucleate favorably on grain boundaries. The number density and size of the precipitates increases with aging.

growth during the solution treatment, while the bimodal basal intensity split along the RD remained, and the texture was not significantly affected. Subsequently, the samples were subjected to an aging treatment in a silicone oil bath at 250°C for a peak aging time of 16 h, followed by water quench. This heat-treated material is referred to as the T6 condition. After the solution treatment phase, aging played little to no role in grain growth but allowed for the precipitation of metastable and equilibrium precipitates throughout the microstructure. In order to study the effects of heat treatment after the solution treatment, various aging times were also studied in addition to the T6 condition. Fig. 1 shows the microstructural evolution during heat treatment, and Fig. 2 shows SEM images of the largest precipitates formed during the T6 aging. The fine precipitates that occur in this condition were characterized using transmission electron microscopy and atom probe tomography, as reported by Sitzmann and Marquis (2015). With increased aging, the precipitates increased in number density and size up to the point that coarsening starts around peak aging of the T6 condition (Sitzmann and Marquis, 2015).

In order to measure the bulk tensile properties, cylindrical tensile specimens were machined in accordance with ASTM standard E8/E8M. Specimens were machined with a low stress turned finish. The samples were designed with the tensile loading direction parallel to the plate rolling direction (RD). The gauge length was 3.175 cm, the gauge section diameter 0.635 cm, and the grip section diameter 1.27 cm. An MTS Landmark servohydraulic load frame with a 1.27 cm collet was used to uniaxially load the cylindrical tensile samples to failure at a displacement rate of 10^{-6} m/s, corresponding to an approximate strain rate of 3×10^{-4} s^{-1}. Displacement was measured using an MTS extensometer (model 634.12 F-2X). Five samples of each heat treatment were tested to failure.

Samples were etched in a solution of 50 ml methanol +6 ml hydrochloric acid +4 ml nitric acid for 3–5 s, and then rinsed with ethanol and blown dry with compressed air prior to the EBSD imaging. This etchant revealed precipitates on the surface but did not preferentially etch the grain boundaries. This is important for in-situ testing, where a deep grain boundary etch could act as a stress concentrator and potentially influence the surface strain field. EBSD was taken using TSL OIM software on a Tescan Mira3 SEM. The OIM software also provides a nominal Schmid factor determined using a direction of loading, which is provided by the operator. The accelerating voltage was 30 kV, the working distance was 18 mm, and the spot size was 61 nm.

The SEM-DIC experiment was conducted on samples with different aging time, and local strain variation was investigated. First, flat dogbone-shaped tensile specimens were produced by machining the specimen blanks using wire electro-discharge machining (EDM). The sample was uniaxially loaded in tension parallel to the rolling direction (RD), and surface deformations were tracked using SEM-DIC. To allow for the characterization of surface strain behavior over a large sampling of grains, 1 mm × 1 mm images were captured at various intervals during plastic deformation. Eighteen 1 mm^2 areas were taken at each strain interval. In order to track these intervals and map EBSD results onto the DIC results, 30 μm micro-indents were marked on the surface in an array. These indents clearly appear underneath the speckle pattern. A four-point projective transformation using the micro-indentations as control points was used to map the EBSD orientation data onto the DIC strain data. The speckle patterns used for DIC were created using 1 μm alumina particles. An example of a speckle pattern is shown in Fig. 3, where the SEM resolution is 4096 × 4096 pixels. The SEM imaging was conducted with 20 kV accelerating voltage, 18 BI, a working distance of 20 mm, and a scan speed of 1 μs/pixel. VIC-2D commercial DIC software was
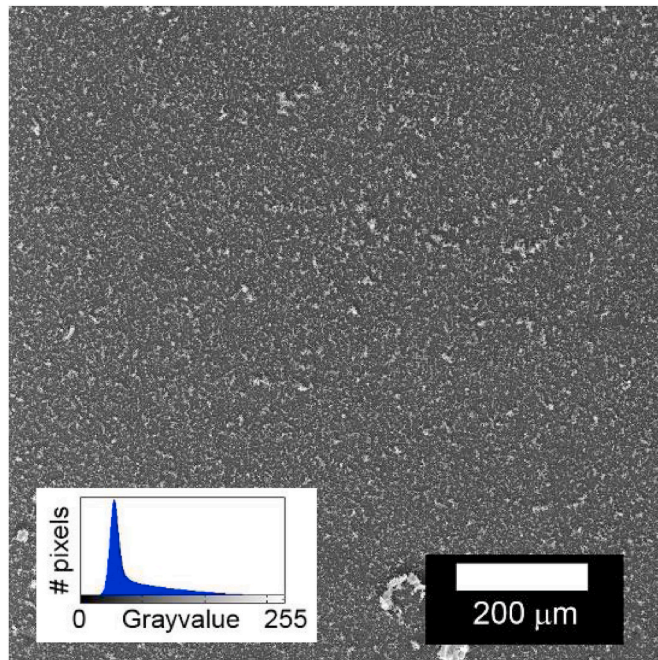

Fig. 3. SEM image of a speckle pattern composed of 1 μm alumina particles on the surface of WE43 Mg alloy. This speckle pattern was used for SEM-DIC.

used to calculate the u and v displacements using a subset size of 51 by 51 pixels and step size of 3 pixels. The analysis settings of an optimized 8-tap interpolation, normalized squared differences criterion, Gaussian subset weights, exhaustive search, low-pass filtering, and incremental correlations were used. The Lagrangian strain was calculated from u and v displacements.

To obtain reliable high-resolution quantitative measurements in an in-situ SEM-DIC test, distortion effects inherent in SEM imaging must be corrected using a calibration sequence (Sutton et al., 2006, 2007a, 2007b; Kammers and Daly, 2013). The most significant of these at the relatively large fields of view used here is spatial distortion. To correct for this distortion, a series of calibration images were taken prior to loading, as outlined by Kammers and Daly (2013). The corrected strain map still shows a mean strain error of 0.2% strain and fluctuations of approximately ±0.75% strain, but it is an improvement over the original data with a mean strain error of 0.4%, fluctuations of ±1% strain, and strong errors on the side of the strain map which exceeds 3.8% strain. Fluctuations appear as a lattice strain pattern that cannot be corrected during calibration. Due to the relatively large fields of view and the large strains induced by plastic loading, drift distortion correction was not necessary for this analysis. Once spatial distortions were quantified, micro-tensile specimens were pulled in tension along the RD to failure, in-situ, pausing the test to collect SEM images of the surface at different strains. The resulting images were processed to calculate full-field u and v displacements, remove spatial distortion errors, calculate the 2-D Lagrangian strain tensor, and map the EBSD data to the strain data.

3. Crystal plasticity finite element simulation

3.1. Crystal plasticity model

The rate-independent crystal plasticity model implemented in PRISMS-Plasticity software (Yaghoobi et al., 2019) was used here for CPFE simulation. The model was originally developed by Anand and Kothari (1996). Here, the plastic deformation is accommodated through slip on prescribed slip systems. The finite deformation formulation is used here. Accordingly, the deformation gradient tensor **F** is described using a multiplicative decomposition as follows:

$$\mathbf{F} = \mathbf{F}^e \mathbf{F}^p \tag{1}$$

where $\mathbf{F}^e$ and $\mathbf{F}^p$ are the elastic and plastic deformation gradient tensors, respectively. The macroscopic velocity gradient tensor **L** can be additively decomposed as below:

$$\mathbf{L} = \mathbf{L}^e + \mathbf{L}^p \tag{2}$$

where $\mathbf{L}^e$ and $\mathbf{L}^p$ are the elastic and plastic velocity gradient tensors, respectively. The plastic velocity gradient tensor can be described using the shearing rate on the slip systems as follows:

$$\mathbf{L}^p = \sum_\alpha \dot{\gamma}^\alpha \mathbf{S}^\alpha \, \mathrm{sign}(\tau^\alpha) \tag{3}$$

where $\dot{\gamma}^\alpha$ is the shearing rate on slip system α, τ^α is the shear stress acting on slip system α, and $\mathbf{S}^\alpha$ is the Schmid tensor for the slip system α, which can be defined as follows:

$$\mathbf{S}^\alpha = \mathbf{m}^\alpha \otimes \mathbf{n}^\alpha \tag{4}$$

where unit vectors $\mathbf{m}^\alpha$ and $\mathbf{n}^\alpha$ denote the slip direction and slip plane normal, respectively, in the deformed configuration.

The resolved shear stress on the slip system α can be obtained using the Cauchy stress tensor $\boldsymbol{\sigma}$ as follows:

$$\tau^\alpha = \boldsymbol{\sigma} \cdot \mathbf{S}^\alpha \tag{5}$$

where $\cdot$ operator denotes the standard inner product of tensors.

In a slip system α, the yield surface can be defined as follows:

$$f^\alpha = |\tau^\alpha| - s^\alpha \tag{6}$$

where s^α is the slip resistance on slip system α. The Kuhn-Tucker consistency conditions govern the plastic deformation for each slip system (Yaghoobi et al., 2019).

The governing equation of slip resistances can be defined as follows:

$$\dot{s}^\alpha = \sum_\beta h^{\alpha\beta} \dot{\gamma}^\beta \tag{7}$$

where $h^{\alpha\beta}$ is the hardening moduli which describes the variation of slip resistance for slip system α due to the slip rate on slip system β. The hardening moduli $h^{\alpha\beta}$ can be described as a power-law relationship, considering the combined effect of work hardening and recovery as follows:

$$h^{\alpha\beta} = \begin{cases} h_0^\beta \left[1 - \dfrac{s^\beta}{s_s^\beta}\right]^{a^\beta} & \text{if } \alpha = \beta \text{(coplanar systems)} \\[2em] h_0^\beta q \left[1 - \dfrac{s^\beta}{s_s^\beta}\right]^{a^\beta} & \text{if } \alpha \neq \beta \end{cases} \tag{8}$$

where q is the latent hardening ratio, h_0^β denotes the hardening parameter for slip system β, s_s^β is the slip resistance at hardening saturation for slip system β, and a^β is a material constant for slip system β, which governs the sensitivity of the hardening moduli to the slip resistance. The numerical implementation of this model has been elaborated in Yaghoobi et al. (2019) and Voyiadjis and Yaghoobi (2019b).

The twinning model implemented in PRISMS-Plasticity software (Yaghoobi et al., 2019) was incorporated, which uses a PTR scheme presented by Tomé et al. (1991). Twin systems are considered as polar pseudo-slip systems which are sheared until they are reoriented. The change in the twin volume fraction $\Delta g^{n,t_i}$, which belongs to a nth Gauss integration point number and i^{th} twinning system, can be defined using the change in the corresponding shear slip of the twin system, i.e., $\Delta\gamma^{n,t_i}$, and a constant S, which is called
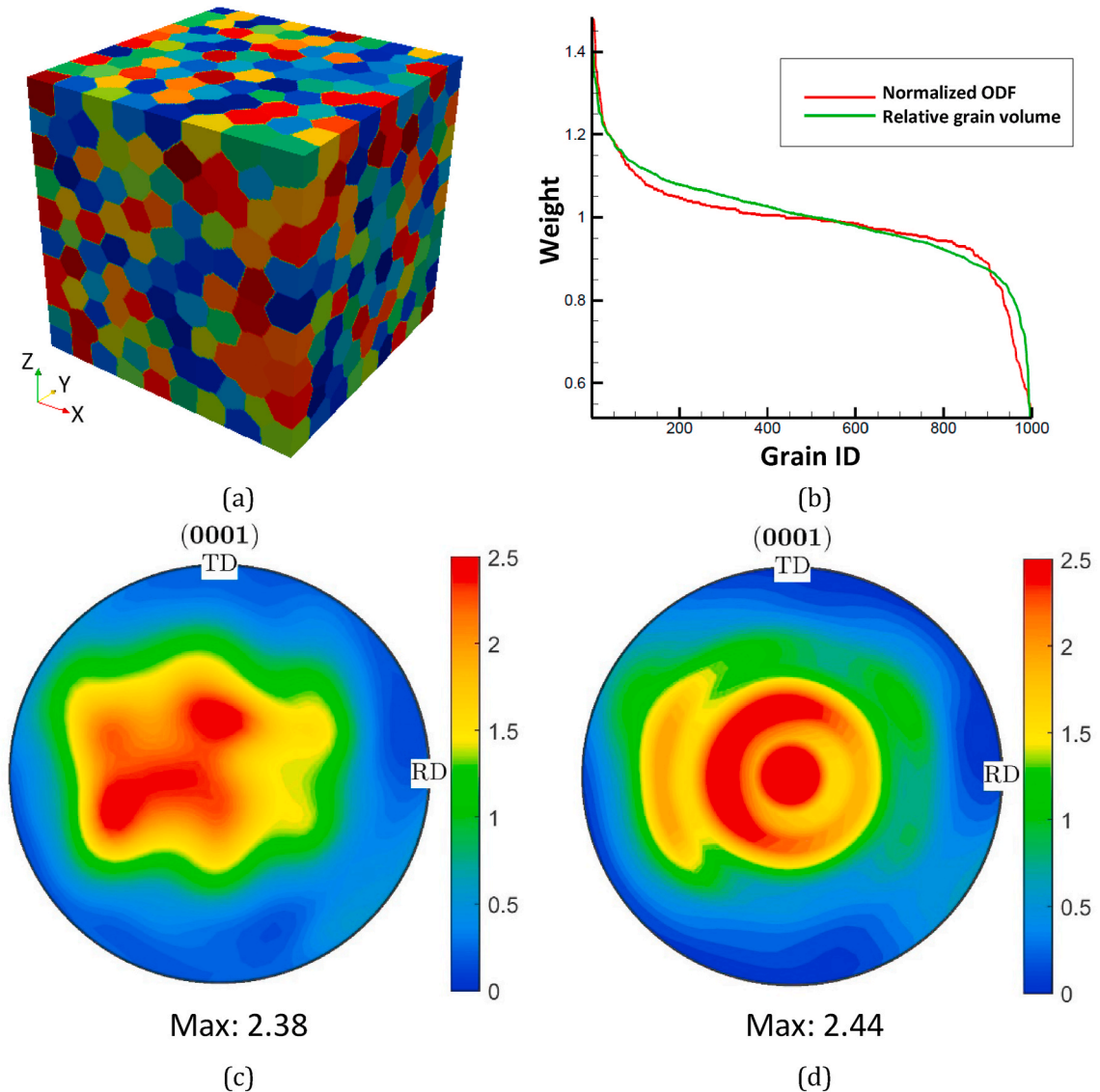

Fig. 4. The microstructure generated using Neper to capture the macro response of the WE43-T6 condition during uniaxial compression and tension: (a) The 3D generated microstructure (b) The texture match for 1000 grains with the ODF for WE43-T6 sample (c) The (0001) pole figure of WE-43-T6 sample from experimental EBSD data (d) The (0001) pole figure of generated WE43-T6 RVE using Neper.

characteristic twin shear strain, as follows:

$$\Delta g^{n,t_i} = \frac{\Delta \gamma^{n,t_i}}{S}$$ (9)

S is calculated as 0.129 in the case of magnesium (Christian and Mahajan, 1995). The accumulative twinning volume fraction at time step T is defined as:

$$g^{n,t_i} = \sum_{\text{timestep}=1}^{T} \Delta g^{n,t_i}$$ (10)

The threshold for the reorientation due to twinning can be described as:

$$F_T = A + B \frac{F_E}{F_R}$$ (11)

where A and B are material constants. These constants describe the threshold for reorientation in the sample and how the threshold varies as the twin volume changes. A and B are calibrated to accurately capture the length of the plateau and the steepness of the subsequent strain hardening during the uniaxial compression test. F_E is the total volume fraction of reoriented Gauss integration points in which the twinning volume fraction reaches the threshold, i.e., $g^{n,t_i} > F_T$. Finally, F_R is the real twinned fraction, which can be defined as follows:

$$F_R = \sum_{n=1}^{N} f^n \sum_{i=1}^{N_{\text{tw}}} g^{n,t_i}$$ (12)

where f^n is the volume fraction of nth Gauss integration point, N is the number of Gauss integration points, and N_{tw} is the number of twinning systems. A Gauss integration point is reoriented due to twinning if $g^{n,t_i} > F_T$. The detailed reorientation procedure can be found in Yaghoobi et al. (2019).

3.2. Construction of representative volume element

In the current work, an open-source software package Neper (Quey et al., 2011) was used to generate the RVEs to simulate the macro response of the polycrystalline WE43-T6 Mg alloy sample during uniaxial tension and compression. The same RVEs have been used for the computation of overall relative activity of the microstructure, which is discussed in section 4.2.2. The RVEs with centroidal Voronoi tessellation were generated using the Lloyds algorithm (Lloyd, 1982). As grain size effects were not considered in the current CPFE simulation framework, centroidal Voronoi tessellation ensured well-shaped and uniformly sized convex cells. The presence of a larger number of grains in the RVE allowed it to map to the experimental texture accurately. Here, the generated RVE for the WE43-T6 Mg alloy sample contained 1000 grains, as shown in Fig. 4 (a). The orientation distribution function (ODF) was obtained from the experimental EBSD data and matched to the microstructure using a texture matching algorithm (Ganesan, 2017) by assigning orientations of independent nodes to individual grains of the microstructure (Fig. 4 b). The assignment of orientation to the individual grains was performed by mapping the relative volume of grains to the normalized ODF values. The comparison of (0001) pole figures for the experimental texture and generated RVE is shown in Fig. 4 (c) and (d). The microstructures generated from Neper were matched to a weakly basal texture, which was similar to the one reported in the experiment.

3.2.1. Texture-matching procedure

The complete orientation space of a polycrystal can be reduced to a smaller subset, called the fundamental region, as a consequence of crystal symmetries. Within the fundamental region, each crystal orientation is represented uniquely by a coordinate, r, the parametrization for the rotation (e.g. Euler angles, Rodrigues vector etc.). The ODF, represented by $A(r)$, describes the volume density of crystals of orientation r. The fundamental region is discretized into M independent nodes. The ODF is normalized to unity over the fundamental region. The normalization is equivalent to the linear constraint. $\sum_{i=1}^{M} q_i A_i = 1$ (b)

In the current work, ODF has been defined by discrete binning in Euler space. The orientations from the EBSD data are used to come up with the ODF function. The ODF is matched to the RVE by assigning the orientations of independent nodes to the individual grains of the microstructure. Fig. 4(b)) shows the texture match for 1000 grains with the ODF for T6 temper. The ODF values ($q_i A_i$) are multiplied by the number of grains (N), it can be seen that $N \times \sum_{i=1}^{M} q_i A_i = N$. Each ODF then is $N q_i A_i$ and contains the approximate number of grains that constitute that orientation. However, two issues occur. Firstly, the volumes of all grains are not equal. Secondly, the values ($q_i A_i$) are in the form of fractions. We split each value of $N q_i A_i$ into equal parts (P_i) by dividing it with its rounded number (eg. 3.3 split into 3 parts of 1.1 each and 3.6 into 4 parts of 0.9 each). The number obtained ranges from 0.6 to 1.4 in our case. These numbers can be directly matched to the relative grain volumes (defined as $N V_i / (\Sigma_i V_i)$, N: no. Of grains, V_i: volume of each grain) of different grains. Larger grains are assigned to orientations of grains with larger P_i values. It is to be noted that a greater number of grains leads to a better match between the curves.

3.3. Boundary value problem

The comparison between CPFE simulation and SEM-DIC experiments is performed by setting up a boundary value problem (BVP) using the EBSD image of the microstructure within the DIC window. The displacement fields in the x and y directions along the microstructure boundary were obtained from the experiment and applied across all the four boundary faces of the microstructure; x = 0, x = a, y = 0, y = b; and it is constrained at the corner (0,0,0) in z-direction as shown in Fig. 14 (a) and (b). . No displacements in z-direction were provided along these four boundary faces. As explained by Githens et al. (2020), the displacement are measured on the surface of the sample, which is traction-free, and therefore a plane-stress assumption is made while setting up the simulation. The slip and twin systems are three-dimensional, and the algorithm to solve for the shear strains and stresses in the slip systems proceeds from a 3-D deformation gradient. Therefore, it is not possible to set up an explicit plane-stress problem similar to 2-D elasticity. Instead, the problem is set-up in 3-D with a plate of very small thickness. A thickness to length ratio of 0.1 was used for all the simulations. Since no variation of variables u and v was expected in the z-direction, a single layer of elements was assumed in the z-direction along with a 200×200 mesh in the x and y directions. Githens et al. (2020) compared the results of the generated columnar sample versus 3D sample and showed that a choice of generalized plane-stress on a columnar grain structure could mimic the SEM-DIC experiment since the surface is traction free.

4. Results and discussion

4.1. Experiment

4.1.1. Macroscopic tensile behavior

Fig. 5 shows the engineering stress versus engineering strain curves for different heat treatment under uniaxial tensile loading. At each heat treatment condition, five samples were tested. Table 1 summarizes the yield strength, ultimate tensile strength, and percent of elongation to failure for the various heat treatments of WE43. The percent of elongation to failure is considered here as a measure of ductility. The results show that the as-received WE43-T5 samples have the highest yield strength, ultimate tensile strength, and ductility. The effects of aging time after the solution treatment of as-received WE43-T5 samples on yield strength, ultimate strength, and ductility during uniaxial tension are shown in Fig. 6. One should note that the y-axis in Fig. 6 is offset (does not start from 0) to improve resolution of the observed differences. Both tensile yield and ultimate strength increased with aging at 250 °C. The ultimate strength increased by 17% from solution treatment (no aging) to peak aging, i.e., T6 condition, while the yield strength increased by 54%. The increase is continuous for both properties. The enhanced properties of WE43-T6 sample compared to the solution treated and underaged samples can be attributed to the fact that as the aging time increases, the precipitates increase in number density and size, as shown in Fig. 2. This is in line with the observations of Sitzmann and Marquis (2015). In the case of ductility, i.e., percent of elongation, the T5 condition has the best performance, while the other heat treatment conditions are not considerably different from each other. As one can see, the difference in the average ductility between the conditions of solution treatment (ST condition) and peak aging (T6 condition) is 4%, which is not considerable. These results suggest that the, within the range studied, aging does not have a significant influence on the ductility. On the other hand, the T5 condition is considerably more ductile than the rest of the heat treatment conditions, which can be attributed to its finer grain size. This is in line with the previous experimental observations of grain size effect
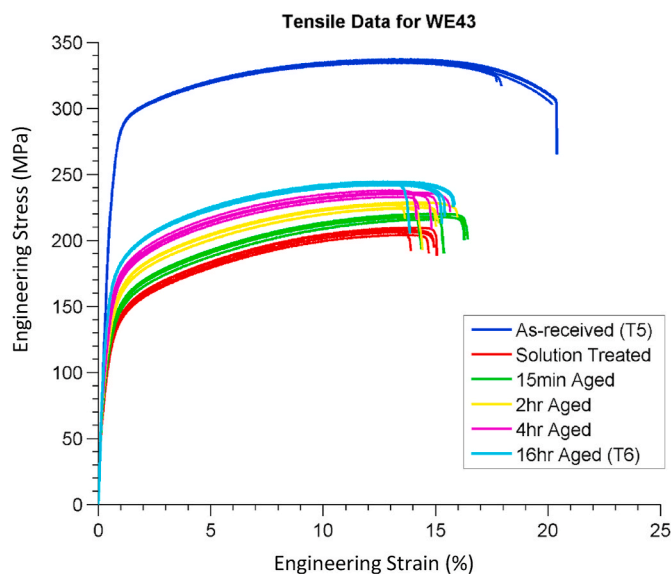

Fig. 5. The WE43 Mg alloy response subjected to various heat treatments during uniaxial tension along RD.

Table 1

Summary of mean values for yield strength, ultimate tensile strength, and percent elongation for the various heat treatments of WE43 Mg during uniaxial tension. $\pm$ values correspond to one standard deviation.

Heat treatment	As-received (T5)	Solution treated	15 min Aged	2 h Aged	4 h Aged	16 h Aged (T6)
Yield Strength (MPa)	265.4	103.2	114.4	123.5	139.1	159.3
	± 0.7	± 1.7	± 2.3	± 2.4	± 4.9	± 0.6
Ultimate tensile strength (MPa)	335.8	206.9	218.5	226.5	235.5	242.9
	± 1	± 2.1	± 1.8	± 1.9	± 1.8	± 1.1
%Elongation	19.31	14.7	15.74	14.83	14.79	15.25
	± 1.4	± 0.48	± 0.88	± 0.87	± 0.62	± 0.83

on ductility in Mg alloys (See, e.g., Mukai et al., 2001; Shi et al., 2013).

4.1.2. In-SEM uniaxial tension

WE43-T5 samples subjected to different heat treatment conditions of solution treated (ST) and aging times of 15 min, 2 h, 4 h, and 16 h, i.e., T6 condition, were subjected to *in-situ* uniaxial tension along the RD, and surface deformations were characterized using SEM-DIC. Full-field strain measurements were analyzed for each heat treatment condition at different macroscopic strain values. For example, in the case of the solution treated sample, the inverse pole figure (IPF) map measured using EBSD and normalized maximum principal strain $\varepsilon_1/\bar{\varepsilon}_1$ maps at various macroscopic strain values of 0.76%, 1.66%, 3.23%, 4.83%, 6.48%, 8.15%, 10.37%, and 12.46% are shown in Fig. 7. In order to study the effect of macroscopic strain on the strain distribution in the plastic region, the probability distribution of normalized maximum principal strain $\varepsilon_1/\bar{\varepsilon}_1$ is further investigated (See Supplementary Information) at applied macroscopic strains of 3.23%, 6.48%, and 10.37% and heat treatment conditions of solution treated and aging times of 15 min, 2 h, 4 h, and 16 h, i.e., T6 condition. The results show that in the plastic region and for all heat treatment conditions, the probability distribution of strain does not change as the globally applied strain increases. This can be visually observed in Fig. 7, in which the spatial distribution of strain at the onset of yield matches the spatial distributions at subsequent loading steps. Martin et al. (2014) reported similar behavior in which in the plastic region, the full-field strain of tensile loaded ZEK100 magnesium alloy did not significantly change as the macroscopic loading increased. Githens et al. (2020) also found a similar trend in the testing of Mg WE43-T5. The lack of change in the spatial distribution of strain indicates that strain heterogeneity does not vary as the macroscopic loading increases within the plasticity region. This can be attributed to the fact that the governing deformation mechanisms, i.e., the active slip systems and their relative activity, do not change in the plastic region as the globally applied strain increases.

As the strain probability distributions do not change with increased macroscopic loading in the plastic region, it is sufficient to focus on one strain interval when comparing the strain probability distributions across different heat treatments. Accordingly, strain maps at the macroscopic strain of 3.23% for all heat treatments are shown in Fig. 8. The full-field strain maps are similar for the solution treated sample and the samples aged for 15 min, 2 h, and 4 h. In the case of sample aged for 16 h, i.e., T6 condition, as shown in Fig. 8 (f), however, the strain distribution contained fewer localized high strains, which are represented by orange and red in Fig. 8, compared to the underaged samples shown in Fig. 8(a–e). To further investigate this, the probability distribution functions of normalized maximum principal strain $\varepsilon_1/\bar{\varepsilon}_1$ at a macroscopic strain of 3.23% for different heat treatments are shown in Fig. 9. The probability distribution function related to the WE43-T6 sample is different from those of other heat treatment conditions. The maximum probability of the T6 condition occurs at a larger strain compared to the other heat treatment conditions. However, at very large strains of $\varepsilon_1 > 2.5\bar{\varepsilon}_1$, the T6 condition shows lower probabilities compared to the others. Furthermore, not only the absolute difference is considerable; the relative difference in probability in the region of high strains is more obvious. For example, the probability of occurrence of a strain with the value of $4\bar{\varepsilon}_1$ in the sample with 15 min aging time is 0.00967, while that is 0.002515 for the T6 condition. This means that the probability of finding a localized strain of $4\bar{\varepsilon}_1$ is ~3.84 times in the underaged sample compared to the T6 condition. Accordingly, the results show that the T6 sample has a more uniform strain map.

4.2. CPFE simulation

4.2.1. Calibration of crystal plasticity parameters

Crystal plasticity parameters were calibrated by optimization using the response of WE43-T6 under uniaxial loading. An initial microstructure was generated, as described in section 3.2 (Fig. 4). The elastic constants of WE43 used by Githens et al. (2020) were incorporated for the WE43-T6 sample, which is presented in Table 2. The crystal plasticity parameters were calibrated by a gradient optimization approach starting from the parameters of WE43-T5 reported by Githens et al. (2020). The goal was to minimize the L2 norm of the error between the experimental and CPFE simulation stress-strain curves. The optimization upper and lower bounds are defined using the theoretical prediction along the available CPFE model calibrations for WE43 Mg alloy, which are elaborated in section 4.4.1. Table 3 presents the optimization bounds provided for calibration of initial slip resistance and corresponding hardening parameters for slip and twining modes of WE43-T6 Mg alloy. Along with the upper and lower bounds, the following constraints were also provided: $1.5\text{CRSS}_{basal} < \text{CRSS}_{prismatic}$; $1.5\text{CRSS}_{basal} < \text{CRSS}_{pyramidal<a>}$; $1.5\text{CRSS}_{basal} < \text{CRSS}_{pyramidal<c+a>}$; $1.5\text{CRSS}_{basal} < \text{CRSS}_{twin<c+a>}$; $1.25\text{CRSS}_{basal} < s_s^{basal}$; $1.25\text{CRSS}_{basal} < s_s^{prismatic}$; $1.25\text{CRSS}_{basal} < s_s^{pyramidal<a>}$; $1.25\text{CRSS}_{basal} < s_s^{pyramidal<c+a>}$ and $a^{\alpha}{}_{basal} = a^{\alpha}{}_{prismatic} = a^{\alpha}{}_{pyramidal<a>} = a^{\alpha}{}_{pyramidal<c+a>} = a^{\alpha}{}_{twin<c+a>}$. The 3D microstructure generated by Neper and matched to the experimental sample's initial texture by a texture matching algorithm was used for the simulations. The crystal plasticity critical
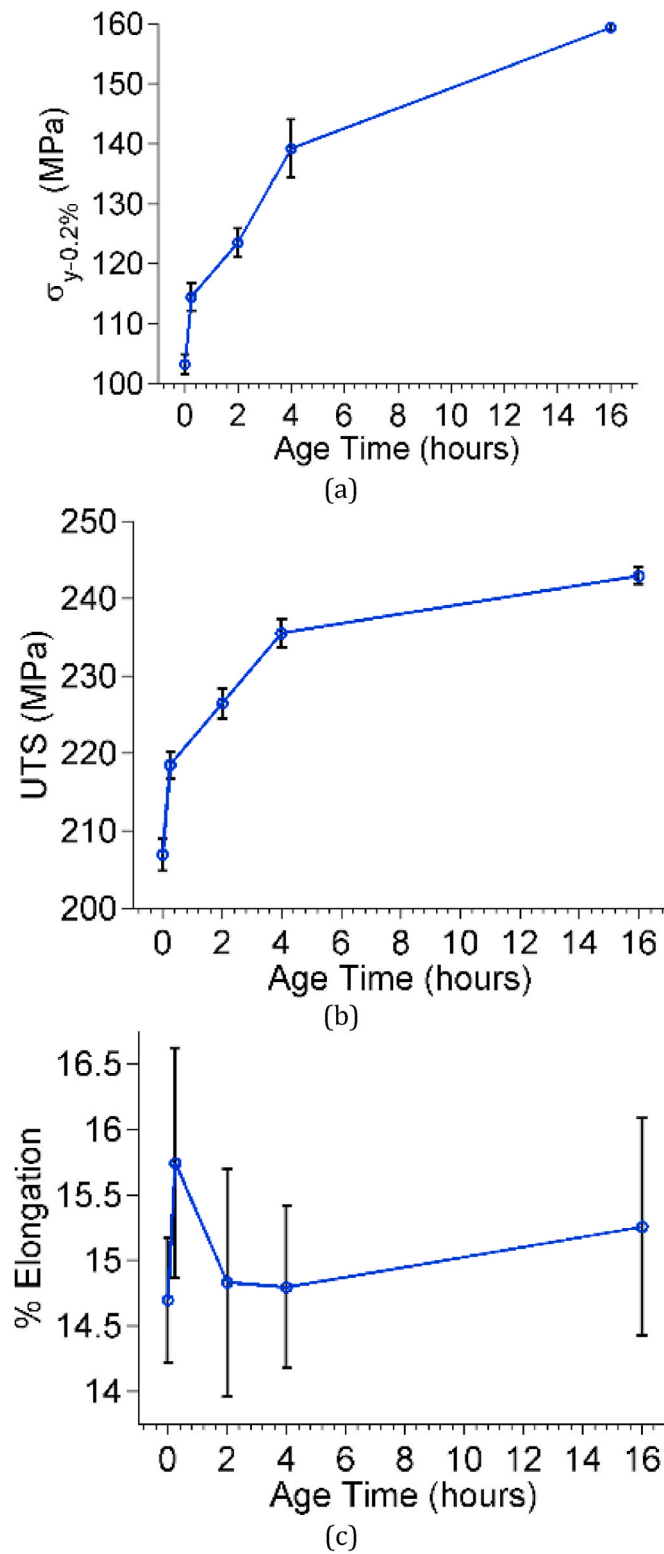
Fig. 6. Effect of heat treatment on the solution treated WE43-T5 samples during uniaxial loading along RD: (a) 0.2% offset yield strength (b) ultimate tensile strength (c) ductility as a function of aging. Note that the y-axis is offset (non-zero) for improved resolution.
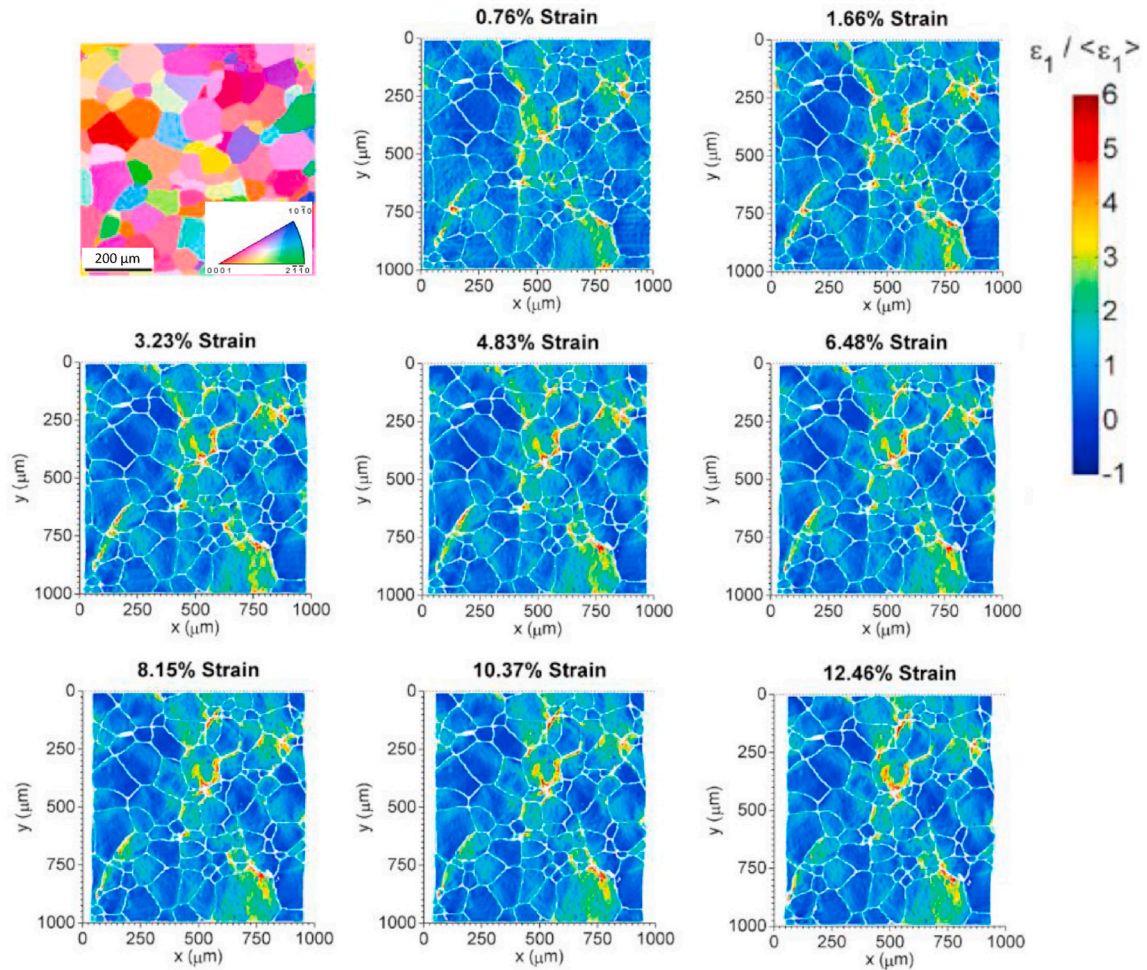
Fig. 7. The inverse pole figure map measured for the Solution Treated (ST) condition using EBSD and normalized maximum principal strain maps of solution treated sample at various macroscopic strain values of 0.76%, 1.66%, 3.23%, 4.83%, 6.48%, 8.15%, 10.37%, and 12.46% during uniaxial tension along RD (x-direction).

resolved shear stress (CRSS) and hardening coefficients were obtained by calibration of uniaxial compression and tension responses in rolling direction, as presented in Table 4. Fig. 10 shows the comparison between a WE43-T6 sample's experimental responses during uniaxial loading along the rolling direction versus those of the CPFE simulation. The simulation successfully captured the experimental results. The crystal plasticity parameters could be calibrated with more accuracy by calibrating with microscale experiments along with multi-objective optimization of using both macroscale and SEM-DIC experiments, such an approach would be considered for a future study. Such a study would also improve the confidence of CRSS values especially for pyramidal $<c+a>$ slip systems. An example of using sensitivity analysis for calibration of crystal plasticity parameters can be found in Sedighiani et al. (2020). The material has considerable tensile anisotropy, as shown in Fig. 11(a), which can be attributed to its weak basal texture. The yield stress is predicted to be higher when loading along the RD and TD directions compared to the ND direction due to the texture anisotropy. The predicted response during loading along RD and TD are similar due to the basal texture symmetry (in-plane). In the case of uniaxial compression, however, Fig. 11(b) shows that the effects of the loading direction are not considerable. The underlying mechanisms of anisotropy during tensile loading and the insensitivity of the compressive response to the loading direction can be unraveled by studying the slip activity of the WE43-T6 condition.

The predicted pole figures for the WE-43 T6 condition during uniaxial tension and compression along the RD, TD, and ND directions are shown in Fig. 12. During uniaxial compression, the $<c>$ axis of the specimen realigns in the direction of applied compression. Fig. 12 (c) shows that the $<c>$ axis moves towards the RD poles during the uniaxial compression along RD. Also, Fig. 12 (e) shows that the $<c>$ axis moves toward the TD poles under compression along TD. The primary mechanism for this texture evolution is twinning. During the tension along TD and RD (Fig. 12 (b) and (d)) and compression along ND (Fig. 12 (g)), twinning is not the favorable deformation mechanisms, and texture does not considerably change. The change in the texture is more obvious in the case of tension along ND (Fig. 12 (f)) compared to the compression along ND (Fig. 12 (g)), which is due to the twinning that occurs during tension along the ND direction. Experimental pole figures for as-received WE43-T5 are available for comparison from Bhattacharyya
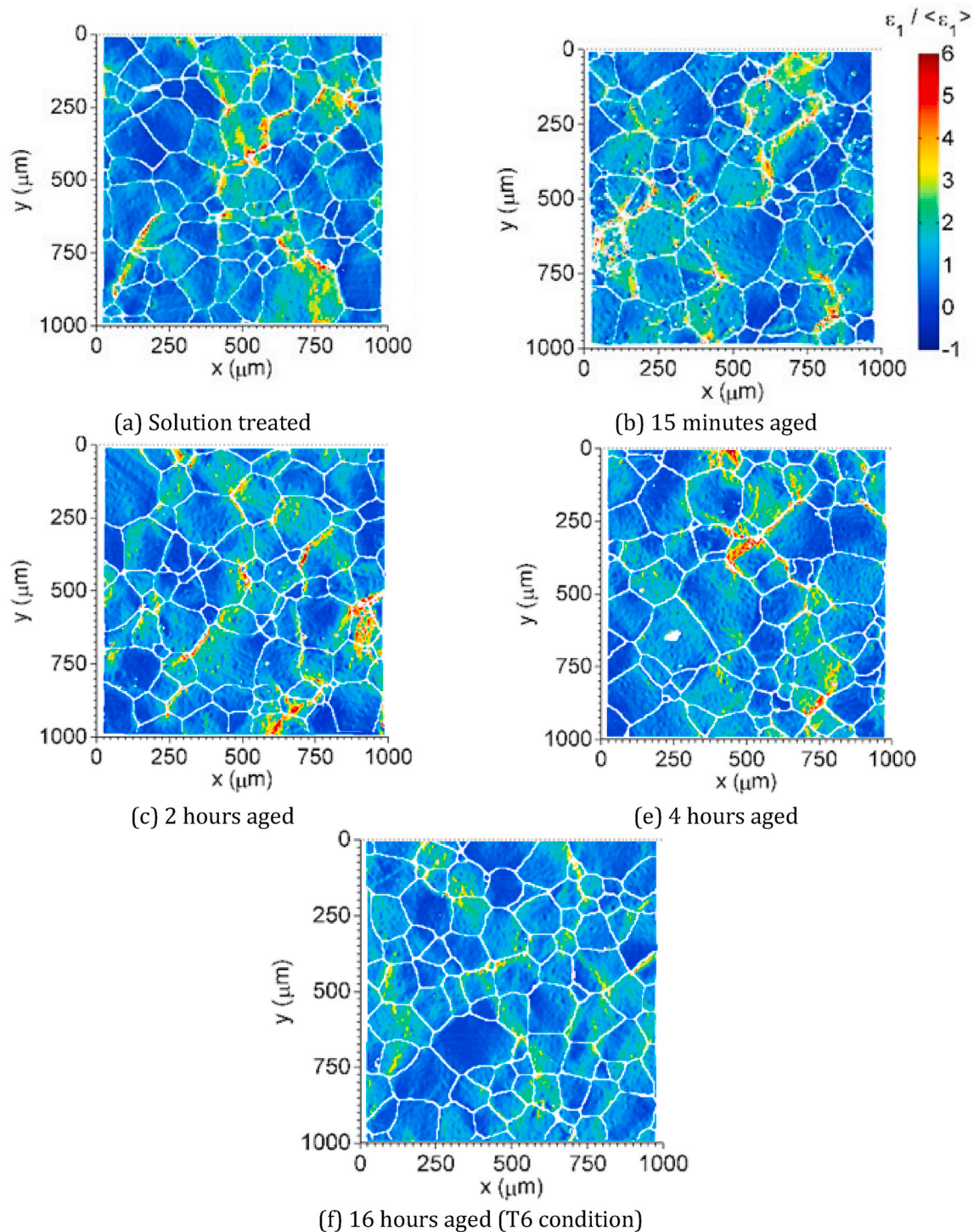
(a) Solution treated

(b) 15 minutes aged

(c) 2 hours aged

(e) 4 hours aged

(f) 16 hours aged (T6 condition)

Fig. 8. The normalized maximum principal strain $\varepsilon 1\varepsilon 1$ maps at the macroscopic strain of 3.23% for different heat treatment conditions of: (a) Solution treated (b) 15 min aged (c) 2 h aged (d) 4 h aged (e) 16 h aged (T6 condition) during uniaxial tension along RD (x-direction).

et al. (2016), and although the heat treatments are different, the textures and slip systems being similar, they are comparable to those in Fig. 12.

4.2.2. Relative activity of the slip systems

To illustrate the underlying deformation mechanisms of stress-strain response and texture evolution shown in Figs. 11 and 12, it is
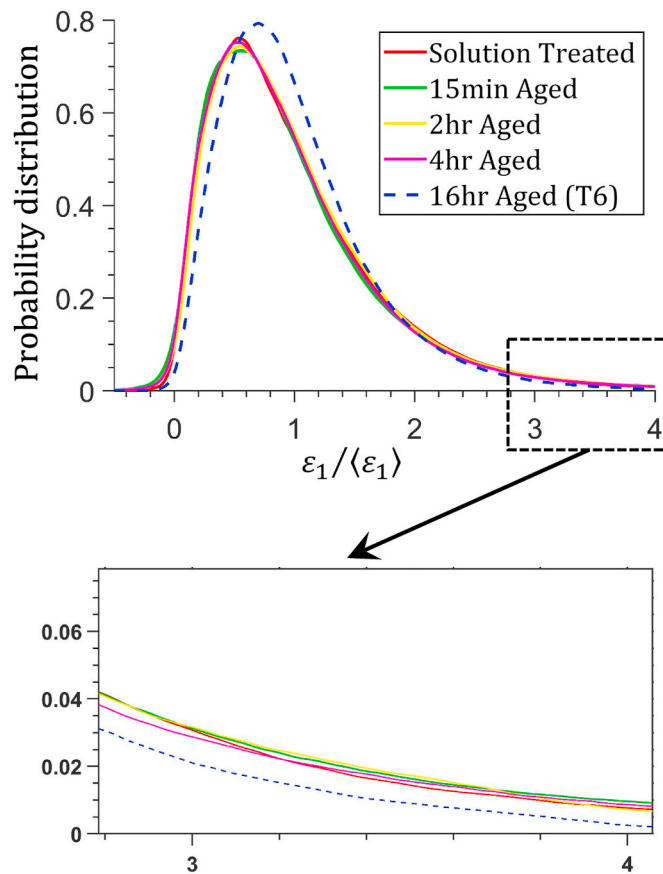
Fig. 9. The probability distribution of normalized maximum principal strain ε1ε1 at the macroscopic strain of 3.23% for different heat treatment conditions of solution treated and 15 min, 2 h, 4 h, 16 h (T6 condition) aging times after solution treatment.

Table 2
The elastic constants (MPa) of WE43-T6 at room temperature.

C11	C12	C13	C33	C44
59,300	25,700	21,400	61,500	16,400

Table 3
Optimization bounds provided for calibration of initial slip resistance and corresponding hardening parameters for slip and twining modes of WE43-T6 Mg alloy.

Mode	s_0^α (MPa)	h_0^α (MPa)	s_s^α (Mpa)	a^α
Basal	35–60	100–1000	35–500	1–3
Prismatic	75–157	100–1000	75–500	1–3
Pyramidal<a>	75–157	100–1000	75–500	1–3
Pyramidal<c+a>	116–252	100–1000	116–500	1–3
Twinning<c+a>	55–90	100–1000	55–500	1–3

useful to study the predicted relative slip activity for all deformation mechanisms. The relative activity of a deformation mode is defined here as the ratio of the total shear strain due to that deformation mode over the total plastic shear accumulated in the microstructure, all integration points are used in FEM elements in the RVE while calculating the ratio, and no information concerning grain orientation or Schmid factor was used in this calculation. Fig. 13 shows the relative activity of the slip modes during tension and compression along the RD, TD, and ND directions. One should note that the elastic region is excluded. In the case of the WE43-T6 condition, basal slip has the lowest CRSS and is most active at low strain levels. The difference between the tensile and compressive responses can be attributed to the twinning mechanism. The only deformation modes which can occur in the case of tensile loading in the *c* direction are either tensile twinning or pyramidal *c* + *a*. Accordingly, in the case of compression along RD and TD, which leads

Table 4
The calibrated values of initial slip resistance and corresponding hardening parameters for slip and twining modes of WE43-T6 Mg.

Mode	s_0^α (MPa)	h_0^α (MPa)	s_s^α (Mpa)	a^α
Basal	47.6	595.0	144.4	2.5
Prismatic	92.2	412.1	289.0	2.5
Pyramidal<a>	104.5	373.2	347.5	2.5
Pyramidal<c+a>	117.3	321.1	304.9	2.5
Twinning<c+a>	84.4	419.3	148.8	2.5

(a)

(b)
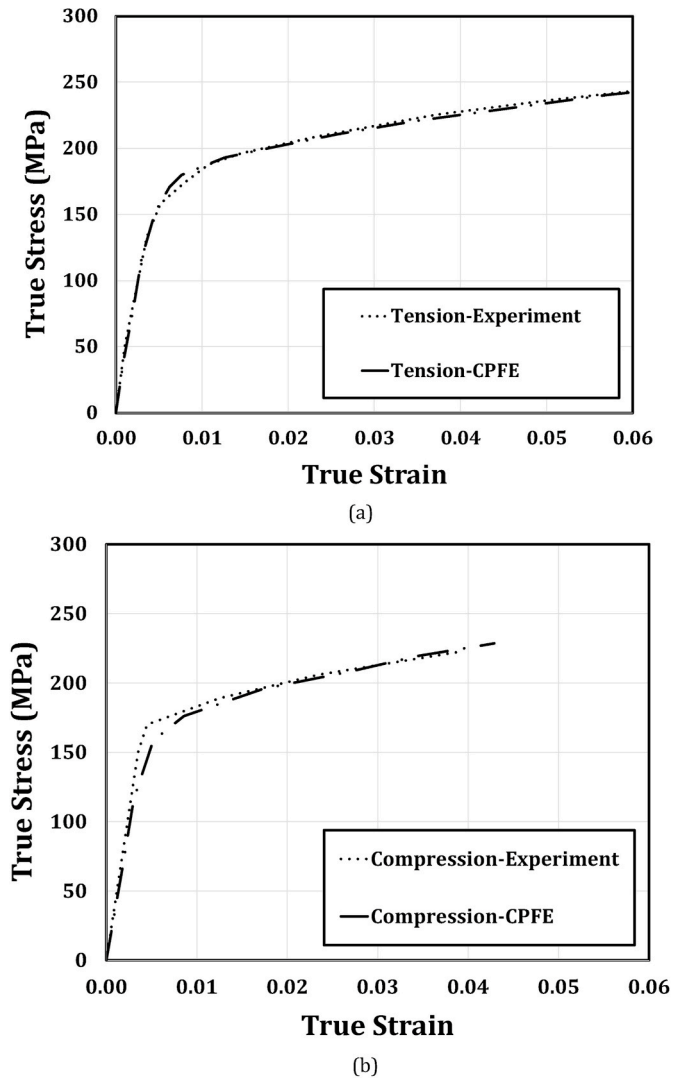
Fig. 10. The responses of WE43-T6 Mg during uniaxial loadings along RD: (a) Tension (b) Compression. The simulation results are compared with the experimental values during uniaxial loadings.

to the tension along c axis, twinning and pyramidal $c + a$ modes compete with each other in which twinning is more active at low strains, and pyramidal $c + a$ more active at higher strains. The anisotropy observed during compression, as shown in Fig. 11 (a), can be attributed to the weak basal texture of RD and TD. As shown in Fig. 13 (b) and (d), twinning is predicted to be activated at lower strains to accommodate the applied strain; however, it is more difficult to activate compared to the basal slip mode. Accordingly, the overall twin activity is lower than that of the basal slip. In the case of loading along ND, on the other hand, more deformation can be accommodated by basal slip compared to those of the RD and TD as shown in Fig. 13 (f). This leads to a lower stress during compression along ND direction compared to those of the RD and TD, which was shown in Fig. 11 (a).

During tension along the RD and TD directions, besides the basal slip mode, the prismatic slip mode accommodates most of the
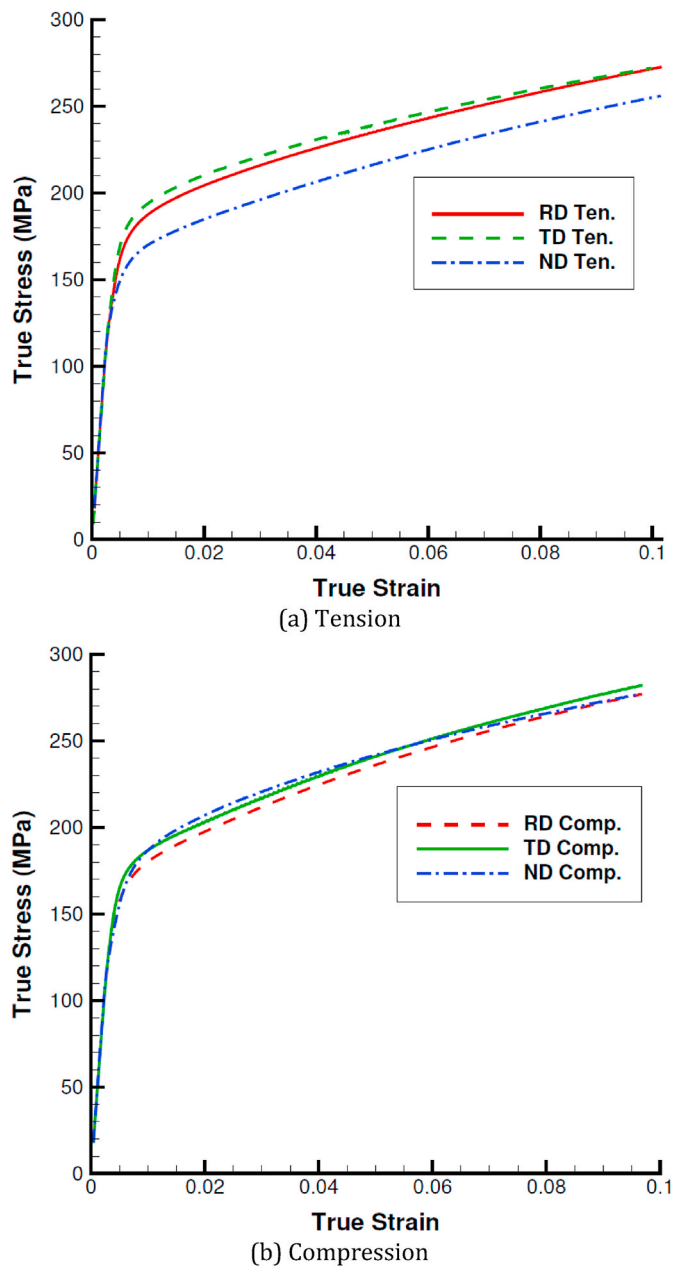
(a) Tension

(b) Compression

Fig. 11. The predicted responses of WE43-T6 Mg during uniaxial loading along RD, TD, and ND loading directions obtained using CPFE simulation: (a) Tension (b) Compression.

applied strain, and only modest twinning is activated. However, in the case of tension along the ND direction, twinning is predicted to be the dominant deformation mode after basal slip for strains lower than 0.08. Prismatic slip becomes more active for strains higher than 0.08.

4.3. Comparison of SEM-DIC and CPFEM

The experimental SEM-DIC results of the WE-43 T6 condition during uniaxial tension are compared with the CPFE simulation using the PRISMS-Plasticity software (Yaghoobi et al., 2019). Here, the aim was to compare the strain fields predicted by CPFE to those experimentally captured by SEM-DIC and to investigate the effect of texture and grain size on the differences between them. The same CPFE parameters calibrated from the 3D synthetic microstructure with macroscopic stress-strain curves were used for these simulations. The nominal basal Schmid Factor (m) (for loading along the RD direction) is also shown in Fig. 14 for the selected points to study the relation between the observed errors and the texture. The displacement maps in the *x* and *y* directions, denoted *u* and *v*
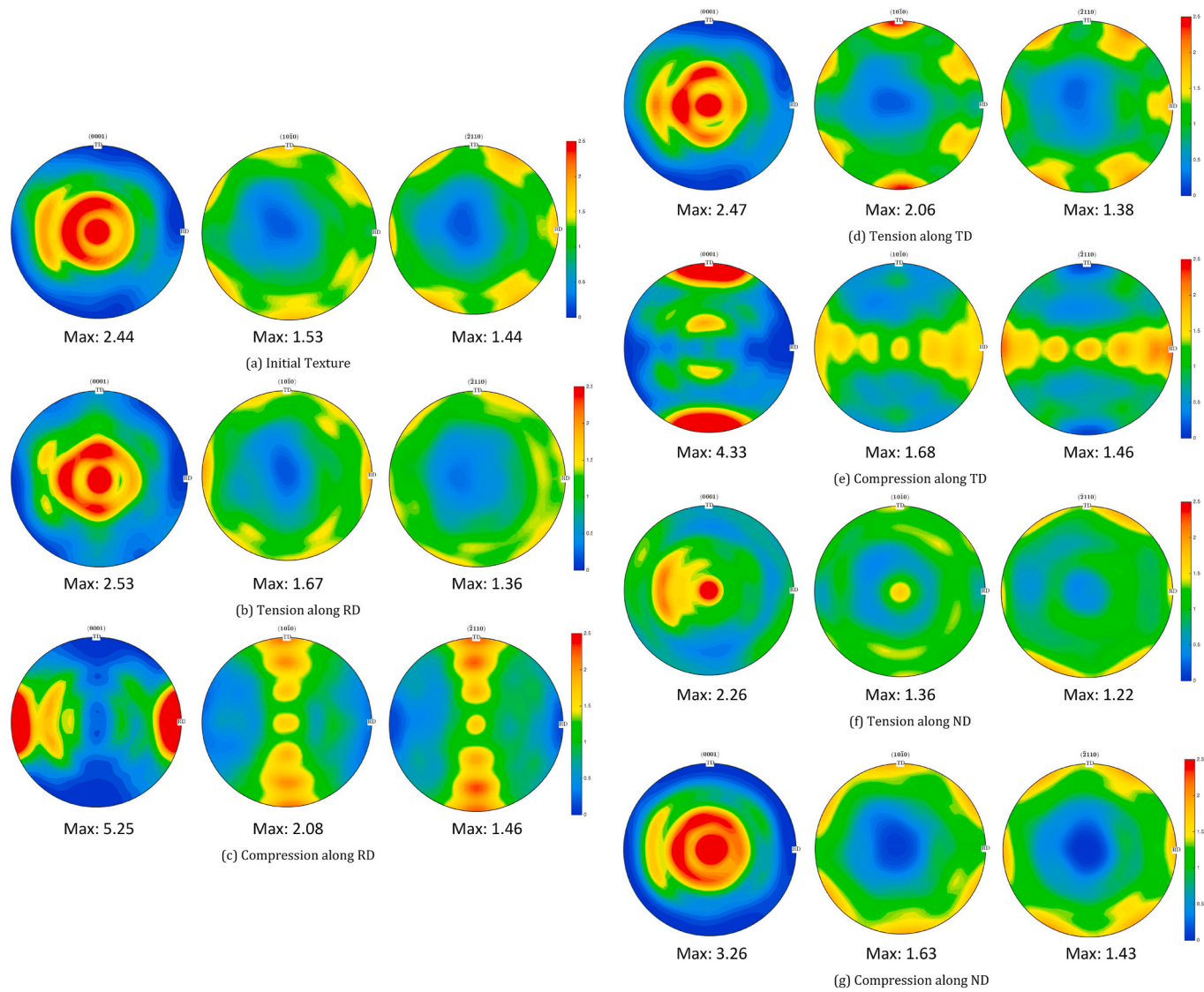
Max: 2.44   Max: 1.53   Max: 1.44

(a) Initial Texture

Max: 2.53   Max: 1.67   Max: 1.36

(b) Tension along RD

Max: 5.25   Max: 2.08   Max: 1.46

(c) Compression along RD

Max: 2.47   Max: 2.06   Max: 1.38

(d) Tension along TD

Max: 4.33   Max: 1.68   Max: 1.46

(e) Compression along TD

Max: 2.26   Max: 1.36   Max: 1.22

(f) Tension along ND

Max: 3.26   Max: 1.63   Max: 1.43

(g) Compression along ND

Fig. 12. The predicted texture of WE-43 T6 during uniaxial loading along different directions at 10% strain: (a) Initial Texture (b) Tension along RD (c) Compression along RD (d) Tension along TD (e) Compression along TD (f) Tension along ND (g) Compression along ND.
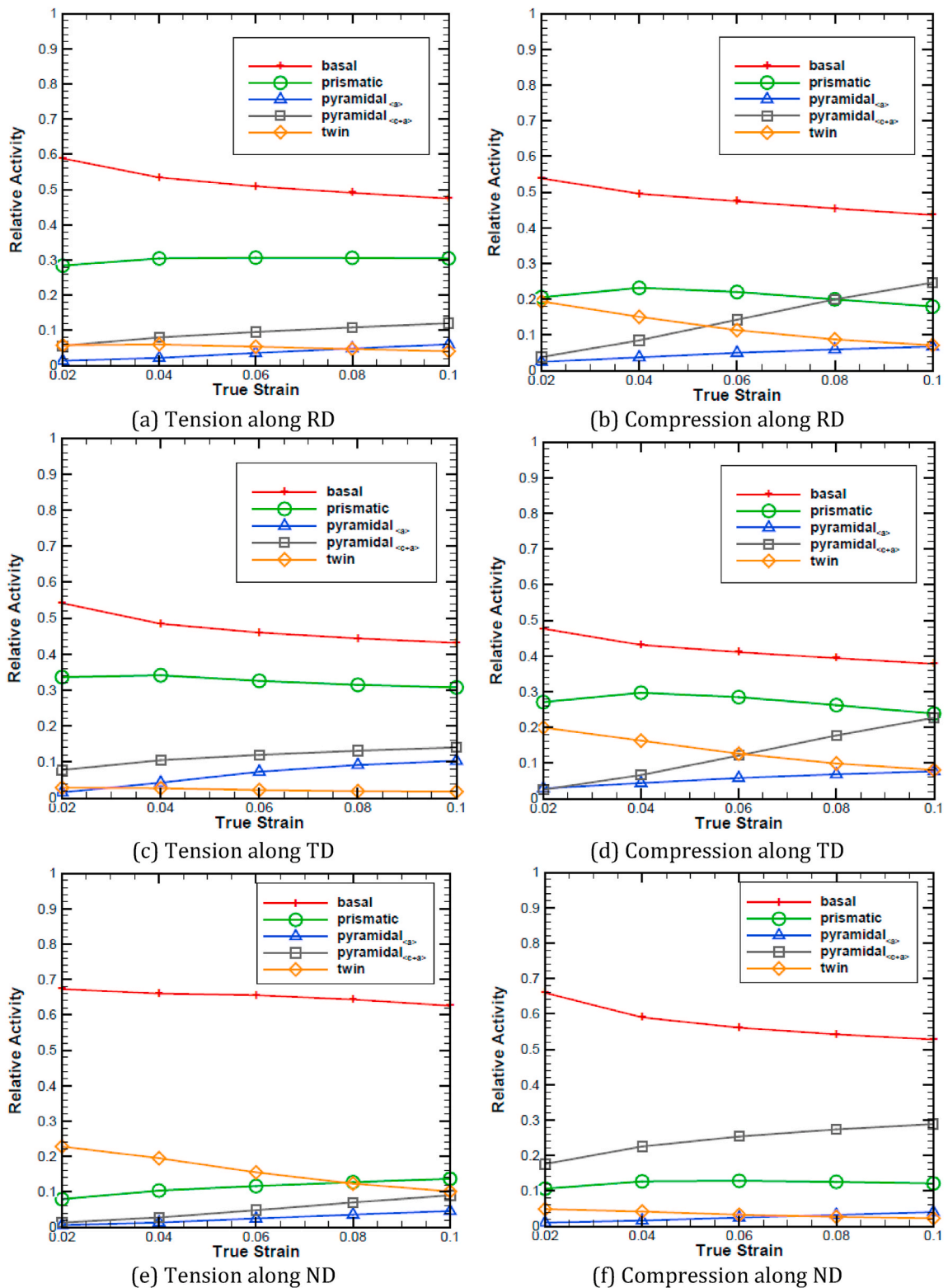
Fig. 13. Predicted relative slip and twinning activity of WE-43 T6 RVE sample during uniaxial loading along different directions: (a) Tension along RD (b) Compression along RD (c) Tension along TD (d) Compression along TD (e) Tension along ND (f) Compression along ND.
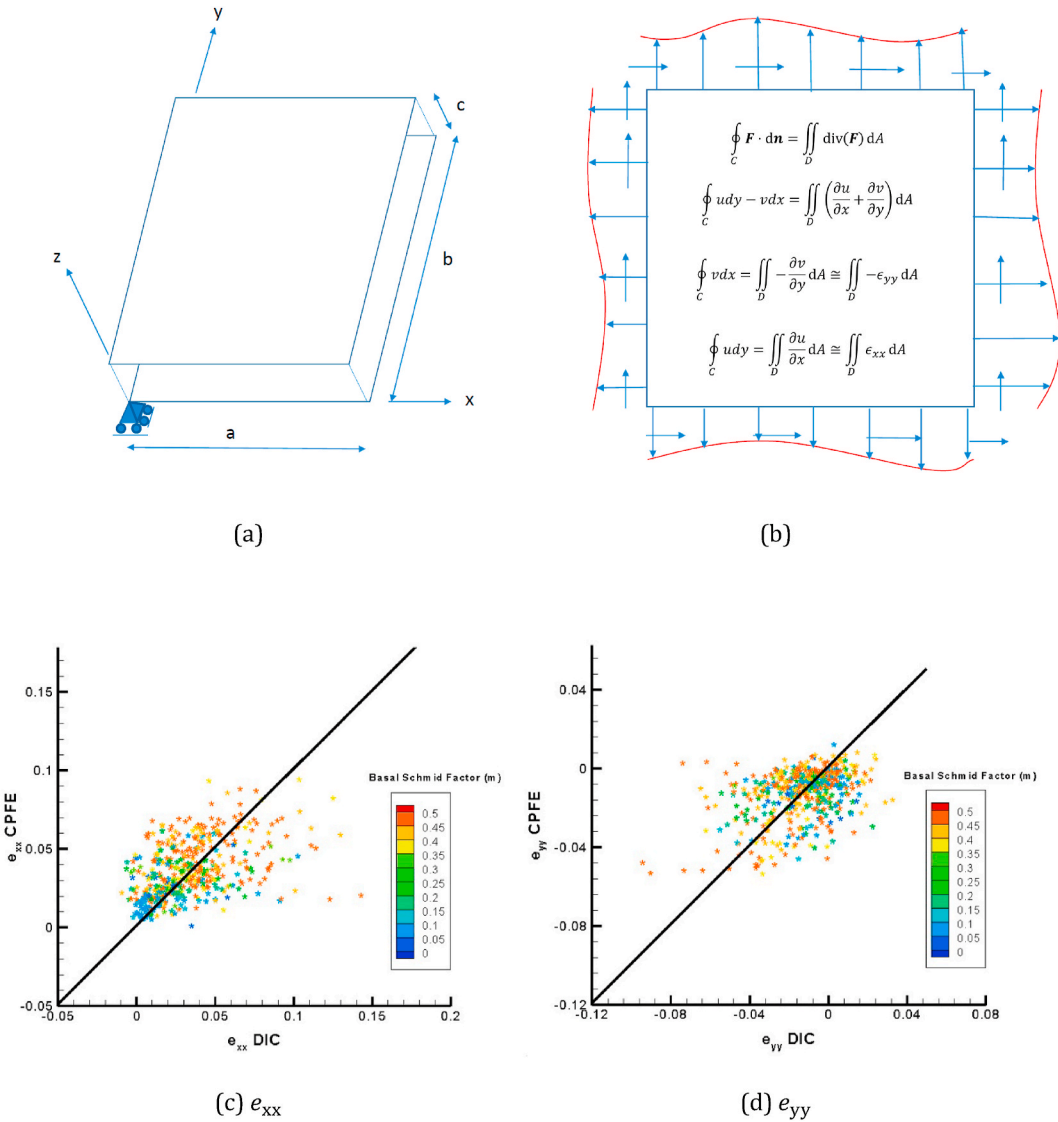
$$\oint_C \boldsymbol{F} \cdot d\boldsymbol{n} = \iint_D \operatorname{div}(\boldsymbol{F})\, dA$$

$$\oint_C u\, dy - v\, dx = \iint_D \left(\frac{\partial u}{\partial x} + \frac{\partial v}{\partial y}\right) dA$$

$$\oint_C v\, dx = \iint_D -\frac{\partial v}{\partial y}\, dA \cong \iint_D -\epsilon_{yy}\, dA$$

$$\oint_C u\, dy = \iint_D \frac{\partial u}{\partial x}\, dA \cong \iint_D \epsilon_{xx}\, dA$$

(a)

(b)

(c) e_{xx}

(d) e_{yy}

Fig. 14. Comparison of CPFE simulations with SEM-DIC experiments in WE-43 T6: (a) CPFE simulation boundary conditions: Both the top and bottom surfaces are made traction free with z-displacement set to zero at (x,y,z)=(0,0,0) (b) Application of 2D Divergence theorem to the boundary value problem where u and v are the displacements in the x and y-direction respectively (c) exx (d) eyy. Comparison of displacement and strain maps are presented for random collection of 800 interior points between CPFE and SEM-DIC during 3.23% uniaxial tensile strain along the x-axis. Schmid Factor is the nominal Schmid Factor for basal slip with macroscopic loading in the RD direction (x-axis).

respectively, obtained by SEM-DIC on a WE-43 T6 sample uniaxially loaded to a 3.23% tensile strain along the *x*-axis (parallel to the macroscopic RD direction) were compared to those obtained by CPFE (See Supplementary Information). In general, the precise boundary conditions of SEM-DIC used in the CPFE simulation limits the errors in the displacement fields.

Fig. 14 (c) and (d) show the comparison between the strain maps of 800 randomly selected interior points obtained by CPFE and SEM-DIC in a WE-43 T6 sample during 3.23% uniaxial tensile strain along the x-axis. Fig. 14 shows the larger scatter in strains, and there is a tendency to significantly underpredict the large values of tensile and compressive strains. This is due to the lack of sharp strain localizations, including twin lamella and slip bands in the CPFE model. Given the same boundary displacement exists for both the DIC data and CPFE model in the way the boundary value problem is set-up, the 2D divergence theorem as shown in Fig. 14 (b) (which derives from generalized Stokes theorem) gives the averaged strain over the microstructure directly from the surface displacements (assuming no cracks in the microstructure). Here, small strain assumption conveys that the averaged strain of the microstructure should be the same for both the experiment and CPFE simulation. In general, by taking derivatives of displacements, the existing error in the displacements are amplified. However, the 2D divergence theorem dictates that if strains are over-predicted in some regions, they should be compensated by under-prediction of strains in some other regions. In DIC data, the strain localizations lead to large displacement jumps, and these are 'smoothed' by the CPFE model as it does not model localizations and discontinuities
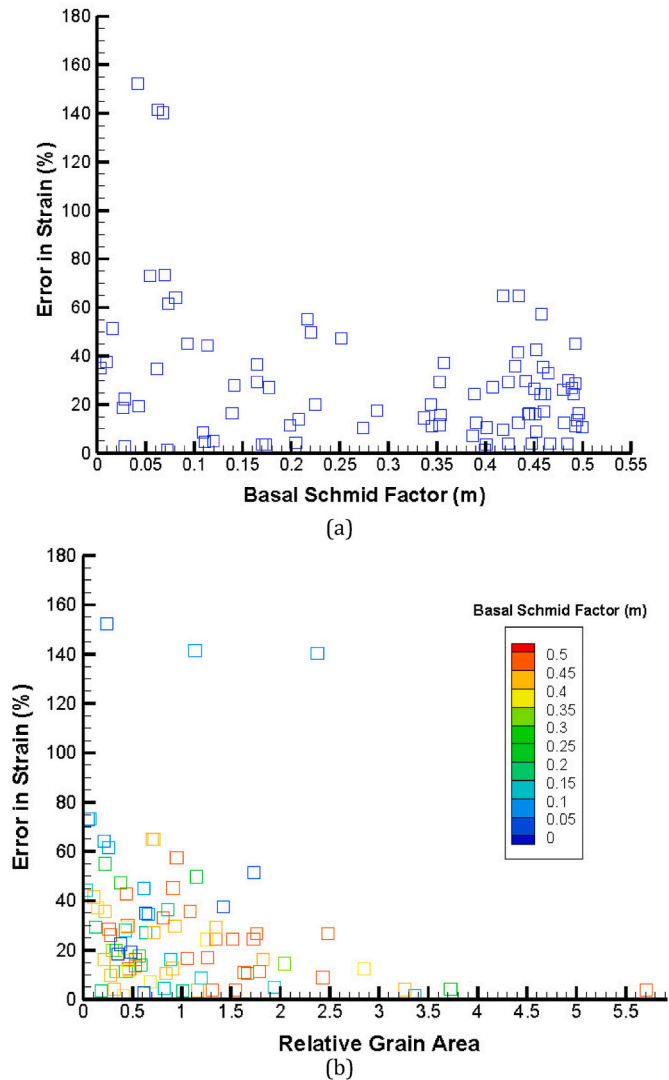
Fig. 15. The error in CPFE prediction of exx as a function of: (a) Basal Schmid Factor (b) Relative grain area AGrainAAverage. The strain values are averaged over each grain. Basal Schmid Factor is the nominal Schmid Factor, and the sample is subjected to the uniaxial tension along RD direction.

finer than the element size used. As expected, based on the 2-D Divergence theorem (Fig. 14 (b)), strains are then overpredicted in other regions to compensate for the underprediction of localized strains. In the next step, the strain values are averaged over each grain to smooth the DIC data. Fig. 15 compares the average error in CPFE prediction of e_{xx} compared to the SEM-DIC data over all grains as a function of nominal basal Schmid factor (m) and relative grain area ($A^{\text{Grain}}/A^{\text{Average}}$), where A^{Grain} is the area of the grain, and A^{Average} is the average area of all simulated grains. Fig. 15 (a) shows that the large error outliers occur for grains with low nominal basal Schmid factor (m). Other than these outliers, the errors look similar across the entire range of Schmid factors for the rest of the grains. In these outlier grains, plastic deformation must be sustained by <c+a> slip mechanisms, and the discrepancy could be due to other factors such as saturation of twinning. Using a more physically based twin model can reduce the errors in those grains. In the case of plotting error versus the grain size, as shown in Fig. 15 (b), there are three error outliers for small and intermediate grain sizes. Excluding these outliers, Fig. 15 (b) shows a clear trend in which as the grain size decreases, the error increases, which can be attributed to the strain gradient effects. In the current CPFE simulation, the strain gradient effects, i.e., dislocation pileup on the grain boundaries, are not included, and including these effects can better predict the strain map in the case of smaller grains. One should note that the contribution of the errors in smaller grains to the average error in stress-strain response is smaller than that of the larger grains because of their area. However, since the local strain variation is also of interest, the error in smaller grains is important to address.

In the next step, two measured microstructural field of views (FOVs) are used for the SEM-DIC/CPFE comparison. Fig. 16 shows the nominal basal Schmid factor (m) distribution and inverse Pole figure (IPF) maps of the selected FOVs. Some grains are alphabetically marked from *A-J* in *FOV1* and *K-T* in *FOV2*, in which the error in strain predicted by CPFE are further investigated. Tables 4 and 5 show the comparison between the strain values obtained by SEM-DIC versus CPFE for the selected grains in *FOV1* and *FOV2*, respectively. In
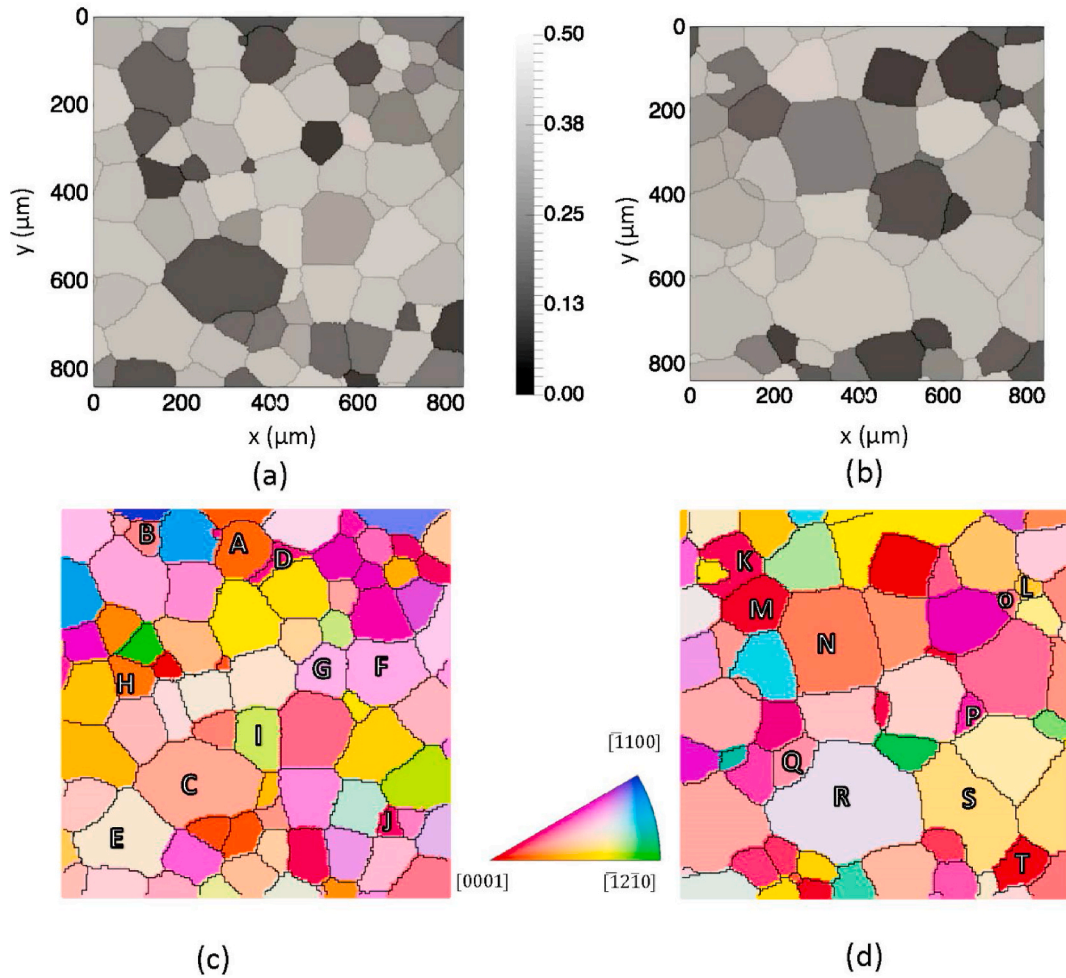
Fig. 16. The initial microstructure for the selected field of views (FOVs): (a) Basal Schmid factor map for *FOV1* (b) Basal Schmid factor map for *FOV2* (c) IPF map for *FOV 1* (d) IPF map for *FOV2*. Some grains are alphabetically marked from *A-J* in *FOV1* and *K-T* in *FOV2*, in which the error in strain predicted by CPFE are further investigated Basal Schmid Factor is the nominal Schmid Factor, and the sample is subjected to the uniaxial tension along RD direction (x-axis).

Table 5
The comparison between the strain values obtained by SEM-DIC versus CPFE for the selected grains in *FOV1*. *m is the nominal Schmid factor for macroscopic uniaxial tension RD (x-axis).*

ID	m	e_{xx}(DIC)	e_{xx}(CPFE)	e_{yy}(DIC)	e_{yy}(CPFE)	Error(e_{xx})%	Error(e_{yy})%
A	0.06	0.009	0.022	−0.001	−0.016	141.4	1363.9
B	0.2	0.041	0.036	−0.023	−0.023	11.5	1.2
C	0.07	0.014	0.015	−0.002	−0.008	1.5	236.2
D	0.4	0.03	0.03	0.005	−0.006	1.4	223
E	0.45	0.018	0.019	−0.003	−0.004	8.9	27.1
F	0.44	0.04	0.047	−0.025	−0.025	16.1	2.8
G	0.44	0.037	0.026	−0.009	−0.009	29.5	0.6
H	0.03	0.022	0.023	−0.014	−0.016	2.8	12.9
I	0.5	0.051	0.042	−0.018	−0.018	16.4	1.4
J	0.08	0.022	0.036	−0.027	−0.027	64.1	0.1

Table 6
The comparison between the strain values obtained by SEM-DIC versus CPFE for the selected grains in *FOV2*.

ID	m	e_{xx}(DIC)	e_{xx}(CPFE)	e_{yy}(DIC)	e_{yy}(CPFE)	Error(e_{xx})%	Error(e_{yy})%
K	0.17	0.043	0.041	−0.024	−0.034	3.5	39.6
L	0.04	0.008	0.02	−0.009	−0.01	152.2	9.4
M	0.11	0.044	0.04	−0.032	−0.035	8.6	9
N	0.2	0.033	0.032	−0.023	−0.025	4.2	6.4
O	0.17	0.028	0.027	−0.034	−0.013	3.5	61.2
P	0.03	0.017	0.02	−0.008	−0.008	18.5	0.4
Q	0.41	0.037	0.027	−0.006	−0.006	27.1	1.2
R	0.47	0.024	0.025	−0.008	−0.01	4	12.5
S	0.45	0.028	0.029	−0.01	−0.014	4	34.2
T	0.44	0.038	0.039	−0.018	−0.018	3.8	1.1

the case of *FOV1*, Table 5 shows that the errors are larger for grains with lower basal Schmid factor (*A, C,* and *J* with basal Schmid factor $m < 0.1$), which is in line with what was shown in Fig. 15. In the case of grain D, although the basal Schmid factor m is large, the error is still large due its small grain size. In the case of *FOV2*, Table 6 shows a trend similar to *FOV1*. Here, the largest errors correspond to the grain *L* which has both a low basal Schmid factor and small grain size. The next largest error belongs to grain *O,* which has a small grain size. The results presented in Tables 4 and 5 are summarized in a histogram plot (See Supplementary Information). The results show that in the cases of both e_{xx} and e_{yy}, the errors are low to moderate (0–30%) for most grains. Only a few outliers that correspond to small area or low basal Schmid factor grains have high error values.

The comparison of strain maps obtained from CPFE versus those of the SEM-DIC experiment in WE-43 T6 alloy sample during 3.23% uniaxial tensile strain along the x-axis are presented in Figs. 17 and 18 for *FOV1* and *FOV2*, respectively. In both cases, although a few strain localizations are smeared, CPFE provides a good reproduction of average strains in several grains, with the best matches seen in larger grains. For a closer comparison of displacement and strain, small windows were extracted from *FOV1* to examine the correlations between the displacements and strains of CPFE and SEM-DIC. The displacement maps of SEM-DIC and CPFE in the selected window of the sample are compared (See Supplementary information). Fig. 19 shows a similar observation for the strain maps. Here, the shear localization pattern in Fig. 19 (a) and (c) to the right of the large grain in the center observed in SEM-DIC are successfully captured using CPFE simulation, as shown in Fig. 19 (b) and (d).

In order to study the evolution of strain maps in the case of CPFE simulation compared to the SEM-DIC experiment, Fig. 20 compares the strain maps of SEM-DIC and CPFE in a WE-43 T6 sample at different uniaxial tensile strain values of 0.76%, 4.83%, and 8.15%. The scale of the strain color map is similar for both CPFE and SEM-DIC, which are located between two maps. The results show that the CPFE can capture many features of the strain map at all considered strain values. Furthermore, as experimentally shown in section 4.1.2 in Fig. 7, the results show that in the range of studied strain values, the pattern of strain maps do not vary for either of SEM-DIC and CPFE as the strain increases.

4.4. Effects of heat treatment

4.4.1. Critical resolved shear stress prediction

In order to study the effect of heat treatments on the CRSS of Mg alloy WE43, the effects of different strengthening mechanisms were investigated here for three conditions of T5, ST, and T6. A Similar methodology was used by Bhattacharyya et al. (2016) to obtain the CRSS of the WE43-T5 alloy. The CRSS for each deformation mode composed of five different contributions of lattice resistance ($CRSS_0$), solute strengthening ($CRSS_s$), grain size effect ($CRSS_g$), forest dislocations ($CRSS_g$), and precipitates ($CRSS_p$) as follows:

$$CRSS = CRSS_0 + CRSS_s + CRSS_g + CRSS_f + CRSS_p \tag{13}$$

Among these mechanisms, the contributions of lattice resistance ($CRSS_0$), solute strengthening ($CRSS_s$), and forest dislocations ($CRSS_g$) can be extracted from T5 data presented by Bhattacharyya et al. (2016). They presented three sets of data for the effects of lattice resistance and solute strengthening ($CRSS_0 + CRSS_s$). First, they obtained ($CRSS_0 + CRSS_s$) directly by summation of lattice resistance and solute effects. However, the solute strengthening was only available for the basal mode (Bhattacharyya et al., 2016). Another two data sets were obtained for samples in the absence of precipitates effects using the EPSC CRSS calculation of Agnew et al. (2013) for large grained casting WE43-ST and Stanford e al. (2014) for Mg - 0.1 at% Y and Mg - 0.6 at% Y binary alloys. To do so, they calculated the contributions of grain boundary and forest hardening and then obtain the effects of lattice resistance and solute strengthening as follows:

$$CRSS_0 + CRSS_s = CRSS - CRSS_g - CRSS_f \tag{14}$$

These three sets of data are incorporated here to capture the contributions of lattice resistance and solute strengthening.
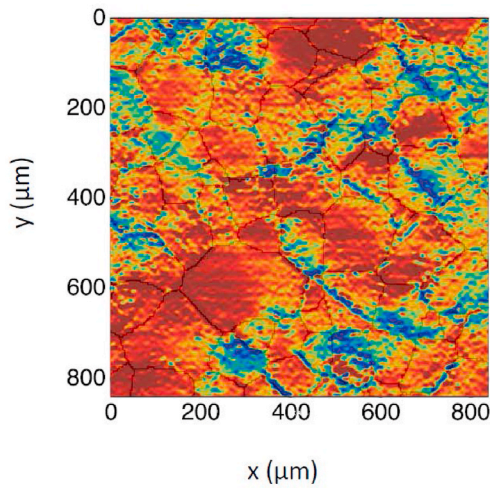
In the case of forest hardening mechanism, the values presented by Bhattacharyya et al. (2016) were incorporated here, which are relatively small compared to other mechanisms. The contributions of grain size effect ($CRSS_g$) was captured using the Hall-Petch relation as follows (Voyiadjis and Yaghoobi, 2019a):
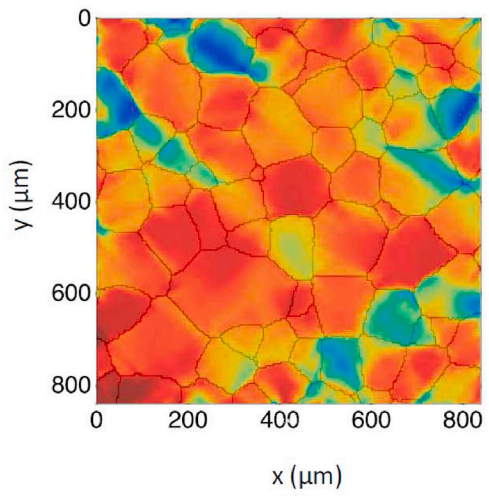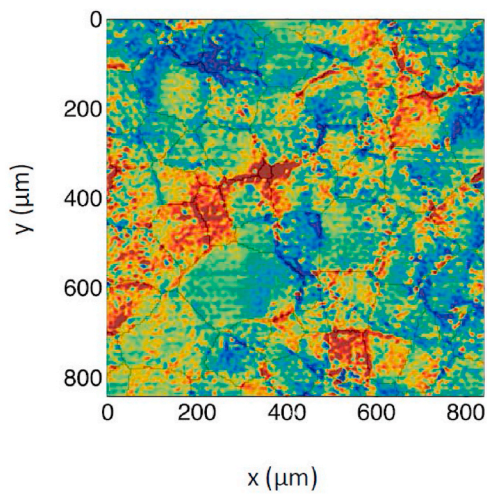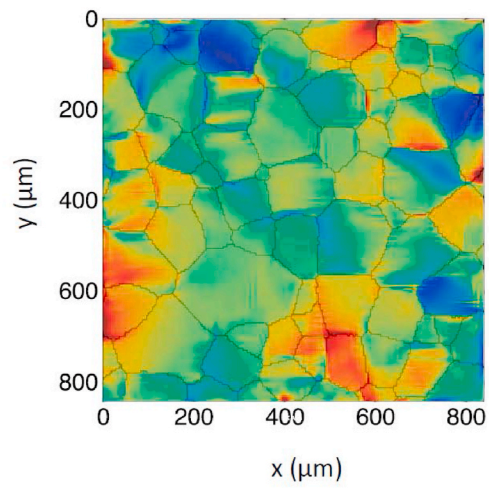
(a)

(b)

(c)

(d)

(e)

(f)
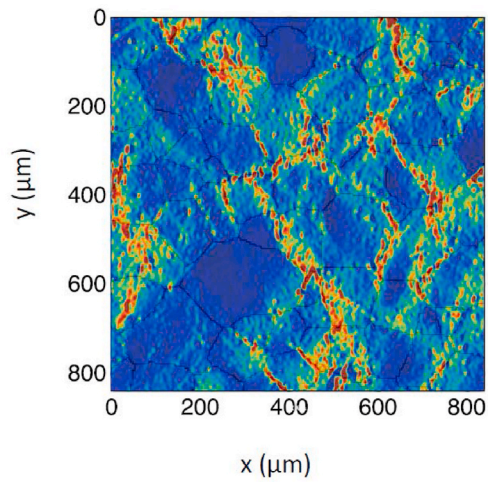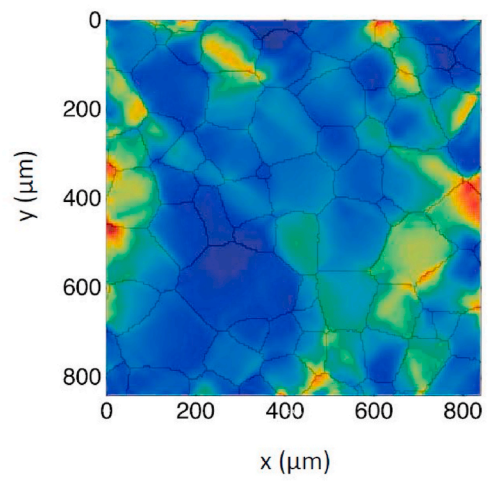
(caption on next page)

Fig. 17. The comparison of strain maps obtained from CPFE versus those of the SEM-DIC experiment in a WE-43 T6 sample during 3.23% uniaxial tensile strain along the x-axis in the case of *FOV1*: (a) exxDIC (b) exxCPFE (c) eyyDIC (d) eyyCPFE (e) exyDIC (f) exyCPFE.

$$CRSS_g = \frac{K}{\sqrt{d}} \tag{15}$$

where K is a macro-Hall-Petch constant, and d is the average grain size of the alloy condition. The constant K dictates the variation of CRSS as the grain size varies. Raeisinia et al. (2011) and Wang and Choo (2014) obtained the constant K for different slip modes in the case of Mg alloys, as presented in Table 7. Accordingly, the contribution of grain size strengthening to the CRSS of T5, ST, and T6 is also presented in Table 7 using the average grain sizes of $d_{T5} = 12\mu m$ and $d_{ST,T6} = 122\mu m$.

Bhattacharyya et al. (2017) comprehensively studied the morphology of the precipitates in WE43 alloy at two different conditions of T5 and T6. Bhattacharyya et al. (2017) observed that the precipitate size distribution and volume fraction in the T6 condition is only slightly larger than that of the T5 condition, and the precipitation strengthening effect is only marginally different. Accordingly, in the current work, it was assumed that the contribution of precipitates to the CRSS in T5 and T6 conditions are similar. Bhattacharyya et al. (2016) calculated this contribution for different deformation modes for WE43-T5 alloy. These values were used in the current study for both T5 and T6 conditions.

The CRSS for each deformation mode was calculated using all the components defined in Eq. (13), which are presented in Table 8. Three different contributions of lattice resistance and solute are represented as $(CRSS_0 + CRSS_s)_1$, $(CRSS_0 + CRSS_s)_2$, and $(CRSS_0 + CRSS_s)_3$, which were obtained using the direct summation, indirect calculation using the EPSC CRSS calculation of Agnew et al. (2013), and indirect calculation using the EPSC CRSS of Stanford et al. (2014). Two sets of data are presented using the Hall-Petch coefficient presented by Raeisinia et al. (2011) and Wang and Choo (2014). Accordingly, three different T5, T6, and ST CRSS data predictions were obtained, as shown in Table 8, each has two values depending on the Hall-Petch coefficients. Platts (2019) used macroscopic compression tests in quasi-static and various strain rates ranging from 400/s-2200/s along RD and ND direction for WE43-T6 and calibrated the CPFE parameters using a VPSC- Voce hardening model. The CRSS of WE43-T6 calibrated by calibrated by Platts (2019) is also presented for comparison in Table 8.

The CRSS presented in Table 8 which were obtained using the available values in the literature and Eqs. 13–15 were used for the optimization of CPFE parameters for WE34 Mg alloy at different conditions. As mentioned in section 4.2.1, the crystal plasticity parameters of WE43-T6 were calibrated by a gradient optimization approach starting from the parameters of WE43-T5 reported by Githens et al. (2020). The maximum and minimum CRSS of T6 condition for each deformation mode presented in Table 8 were used as upper and lower bounds for this optimization, respectively, as shown in Table 3. Due to lack of information for Pyramidal<a>, its upper and lower bounds are assumed to be similar to those of the prismatic mode. The calibration presented by Githens et al. (2020) for the T5 condition and the current calibration for the T6 condition, i.e., $T5 - CRSS_*$ and $T6 - CRSS_{**}$, respectively, are listed in Table 8.

The CRSS for ST condition was predicted here using the $T5 - CRSS_*$ and $T6 - CRSS_{**}$ calibrations by subtracting the solute strengthening contribution, which are denoted in Table 8 as $ST - CRSS_a$ and $ST - CRSS_b$, respectively. The CPFE parameters are calibrated using the uniaxial tension along RD using the described optimization method. $ST - CRSS_a$ and $ST - CRSS_b$ were used as upper and lower bounds for this optimization, as shown in Table 9. Table 10 presents the calibrated values of initial slip resistance and corresponding hardening parameters for slip and twining modes of WE43-ST Mg alloy. Fig. 21 compares the CPFE prediction versus the experimental results of WE43-ST sample during uniaxial tension along RD. The results show that the CPFE model can successfully captured the tensile response observed in the experiment.

The stress-strain responses of the T5 and T6 conditions are also presented in Fig. 21 to summarize the effects of heat-treatment on the response of WE43 sample. As mentioned earlier in section 4.1.1, the T5 condition exhibits a higher yield strength, ultimate strength, and ductility (Table 1). As shown in Eq. (13) and Table 8, the two most decisive factors in this analysis are contributions of grain size $CRSS_g$ and precipitates $CRSS_p$. The grain size increases from $d_{T5} = 12\mu m$ in the as-received T5 condition to $d_{ST} = 122\mu m$ after the solution heat treatment, while it does not change with the subsequent aging time, i.e., $d_{ST} = d_{T6}$. Furthermore, as shown in Fig. 2, after the solution heat treatment (ST condition), the precipitates density and size increase with the aging time, which was also reported by Bhattacharyya et al. (2017). Also, Bhattacharyya et al. (2017) observed that the precipitation strengthening effect is only marginally different for T5 and T6 conditions and thus this difference was neglected in the current work.

One can elaborate on the underlying mechanisms of heat treatment effects on WE43 alloy presented in Fig. 5 using Eq. (13). The differences between the responses of underaged samples and the T6 sample are due to the evolution of precipitates. As the aging time increases, the precipitate density and size increases (Fig. 2). Accordingly, the difference between the responses from T6 condition to ST can be attributed to precipitate strengthening. However, considering the observations of Bhattacharyya et al. (2017), the difference between T6 and T5 condition can be mainly ascribed to the grain size effect. As shown by Raeisinia et al. (2011) and Wang and Choo (2014), the Hall-Petch coefficient should be separately derived for each slip system. One can then use Eq. (15) to capture the Hall-Petch coefficient as follows:

$$K = \left(CRSS_{|d_{T5}} - CRSS_{|d_{T6}}\right)\frac{\sqrt{d_{T5}}\sqrt{d_{T6}}}{\left(\sqrt{d_{T6}} - \sqrt{d_{T5}}\right)} \tag{16}$$

Table 11 presents the Hall-Petch constant K for different slip systems using the calibrated values of T5 and T6, i.e., $T5- CRSS_*$ and $T6 - CRSS_{**}$. The values from the studies of Raeisinia et al. (2011) and Wang and Choo (2014) are also included in Table 11. The results show that higher Hall-Petch constants were obtained in the current work compared to the work of Raeisinia et al. (2011) and
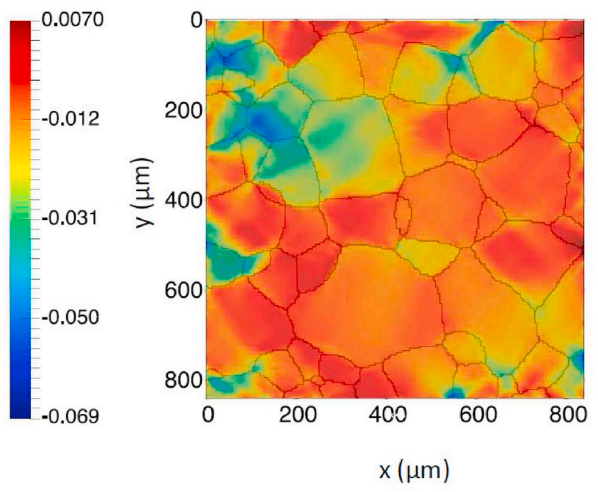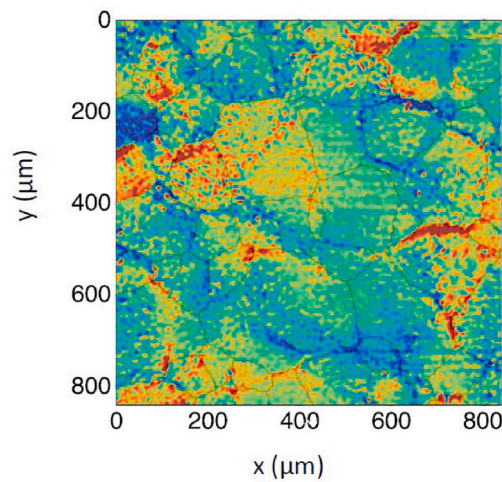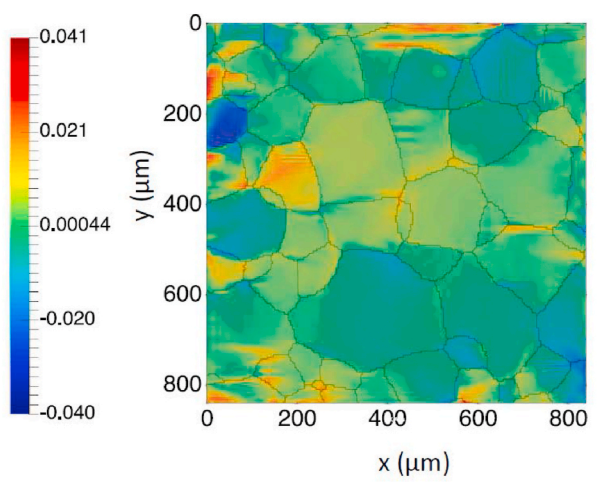
(a)

(b)

(c)

(d)

(e)

(f)

(caption on next page)
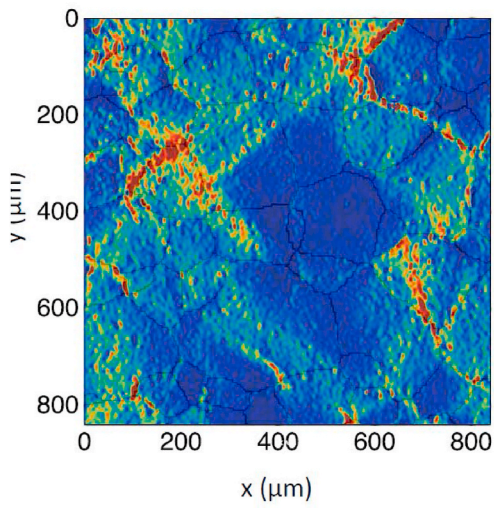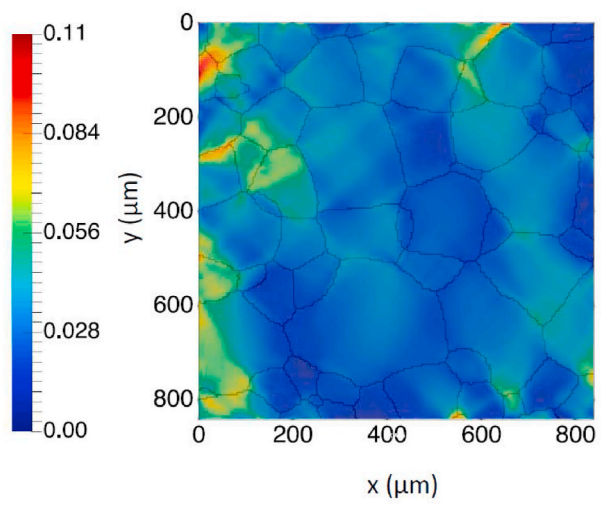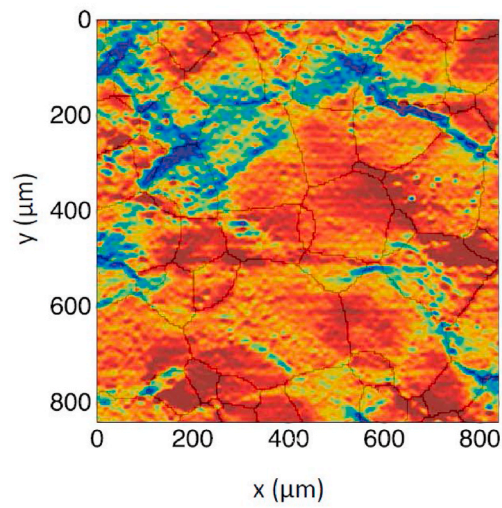
Fig. 18. The comparison of strain maps obtained from CPFE versus those of the SEM-DIC experiment in a WE-43 T6 sample during 3.23% uniaxial tensile strain along the x-axis in the case of *FOV2*: (a) exxDIC (b) exxCPFE (c) eyyDIC (d) eyyCPFE (e) exyDIC (f) exyCPFE.

(a) e_{xx} (DIC)

(b) e_{xx} (CPFE)

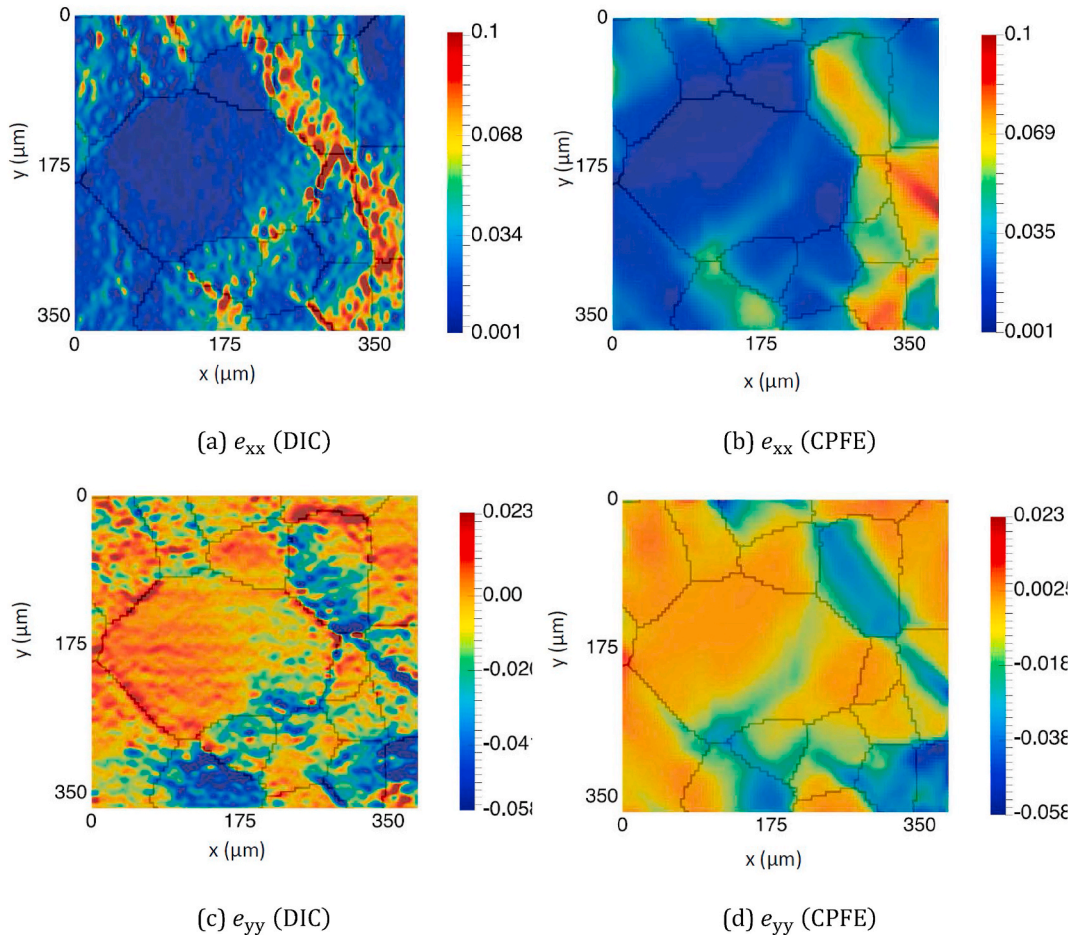(c) e_{yy} (DIC)

(d) e_{yy} (CPFE)

Fig. 19. The comparison of strain maps obtained from SEM-DIC experiment and CPFE simulation in the WE-43 T6 sample during 3.23% uniaxial tensile strain along the x-axis: (a) exx DIC (b) exx CPFE (c) eyy DIC (d) eyy CPFE.

Wang and Choo (2014).

4.4.2. Relative activity of slip systems

The predicted relative slip activity of WE-43 T6 alloy during uniaxial tension along TD obtained in section 4.2.2 is compared with those of the WE-43 T5 condition reported by Githens et al. (2020). The crystal plasticity parameters in Githens et al. (2020) were calibrated by a gradient optimization approach starting from the parameters of WE43-T5 reported by Bhattacharyya et al. (2016) and Stanford et al. (2014). Similar to the current study, the 3D microstructure generated by Neper and matched to the experimental sample's initial texture by a texture matching algorithm was used for the calibration. The crystal plasticity critical resolved shear stress (CRSS) and hardening coefficients were obtained by calibration of uniaxial compression and tension responses in rolling direction, as presented in Githens et al. (2020). These parameters were validated with microscale SEM-DIC experiments and corresponding CPFE simulations and parametric studies were also conducted on effect of CRSS. Fig. 22 compared the relative slip activity of T5 and T6 conditions during uniaxial compression and tension. In both T5 and T6 conditions, basal has the lowest CRSS and is most active at low strain levels. In the case of the T5 condition sample during uniaxial tension, pyramidal $<a>$ is the most active slip mode beside the basal. After basal and pyramidal $<a>$, prismatic and pyramidal $<c+a>$ becomes the next active slip modes. Twinning is slightly active at low strain during tension loading. The pyramidal $<a>$ activity in the T6 condition is considerably lower than that of the T5 condition. Also, the pyramidal $<c+a>$ activity in the T6 condition is slightly lower than that of the T5 condition. However, the prismatic activity in the T6 condition is considerably higher than that of the T5 condition. In the case of the T6 condition sample during uniaxial tension, after the basal slip, prismatic is the most active slip mode. After basal and prismatic, pyramidal $<c+a>$ becomes the
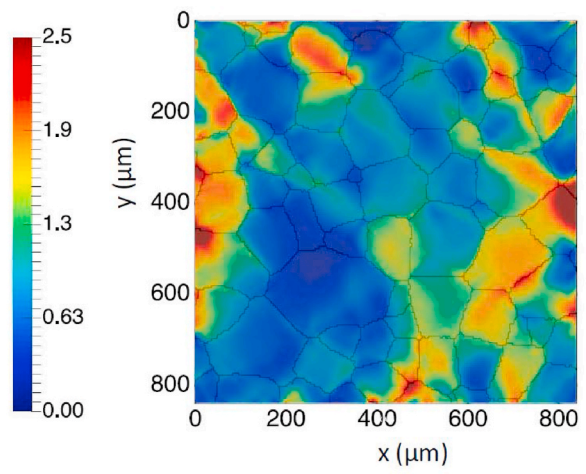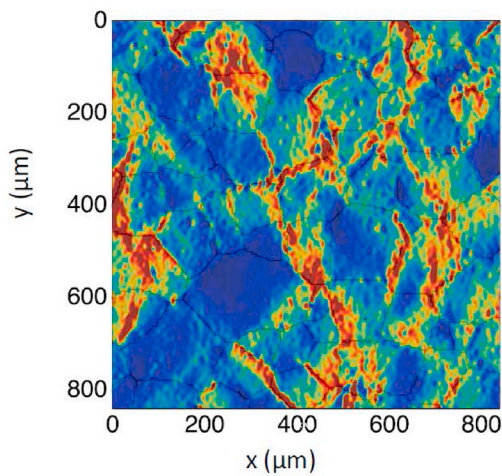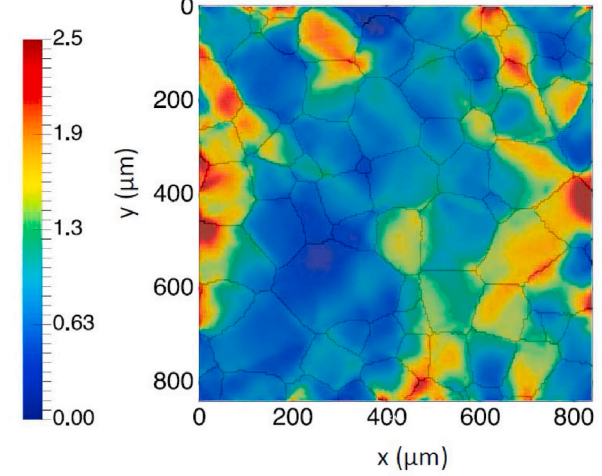
(a)

(b)

(c)

(d)

(e)

(f)
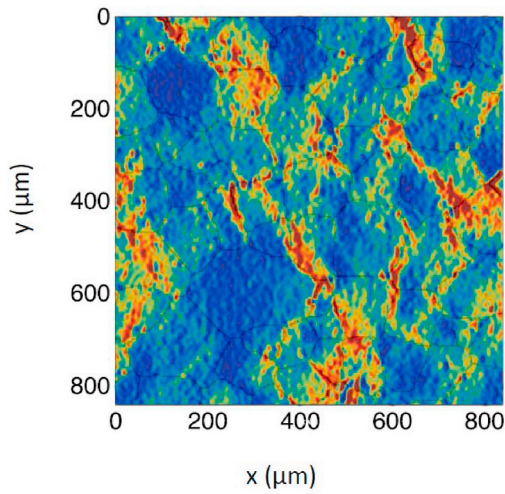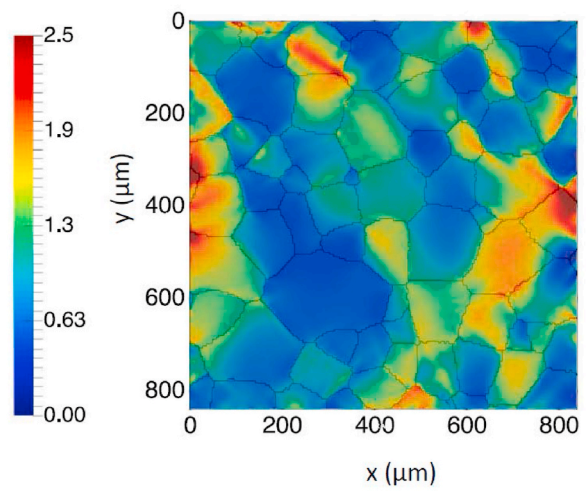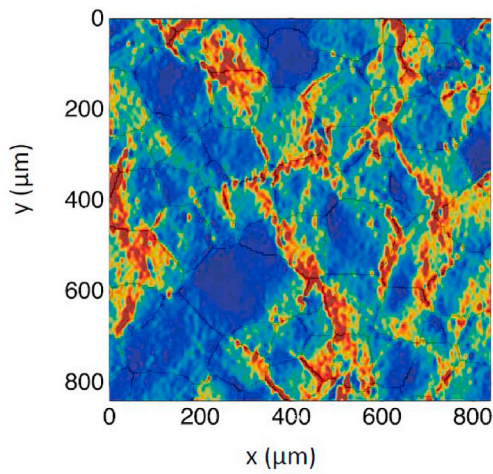
(caption on next page)

Fig. 20. The comparison of relative strain exx maps obtained from SEM-DIC experiment and CPFE in a WE-43 T6 sample at different uniaxial tensile strain values: (a) strain = 0.76% -DIC (b) strain = 0.76% -CPFE (c) strain = 4.83% -DIC (d) strain = 4.83 %- CPFE (e) strain = 8.15% -DIC (f) strain = 8.15% -CPFE.

Table 7
The grain size strengthening contribution to CRSS of T5, ST, and T6 using the Hall-Petch constant K provided by Raeisinia et al. (2011) (first value) and Wang and Choo (2014) (second value).

Mode	K (MPa × mm$^{1/2}$)	T5-CRSS$_g$ (MPa)	ST, T6-CRSS$_g$ (MPa)
Basal	0.42, 2.61	3.83, 23.83	1.20, 7.47
Prismatic	3.72, 5.54	33.96, 50.57	10.65, 15.86
Pyramidal<c+a>	4.71, n/a	43, n/a	13.48, n/a
Twinning<c+a>	n/a, 3.48	n/a, 31.77	n/a, 9.96

Table 8
The theoretical predictions of CRSS prediction of WE43 Mg alloy for different conditions of ST, T5, and T6. Three different contributions of lattice resistance and solute are represented as CRSS0+CRSSs1, CRSS0+CRSSs2, and CRSS0+CRSSs3, which were obtained using the direct summation, indirect calculation using the EPSC CRSS calculation of Agnew et al. (2013), and indirect calculation using the EPSC CRSS calculation of Stanford e al. (2014). Two different Hall-Petch constant sets provided by Raeisinia et al. (2011) (first value) and Wang and Choo (2014) (second value) are considered. T6-CRSS PLATT is the CRSS calibration for WE43-T6 by Platts (2019). T5-CRSS * is the CRSS calibration for WE43-T5 by Githens et al. (2020). T6-CRSS ** is the CRSS calibration of WE43-T6 for the current work. ST-CRSS a and ST-CRSS b are the indirect calculation of WE43-ST using T5-CRSS * and T6-CRSS **, respectively.

Mode	Basal	Prismatic	Pyramidal<c+a>	Twinning<c+a>
(CRSS$_0$+CRSS$_s$)$_1$ (MPa)	8.8	48	40	8
(CRSS$_0$+CRSS$_s$)$_2$ (MPa)	11, 3	65, 59	114, n/a	n/a, 73
(CRSS$_0$+CRSS$_s$)$_3$ (MPa)	15, 6	112, 104	176, n/a	n/a, 80
T5-CRSS$_g$ (MPa)	3.83, 23.83	33.96, 50.57	43, n/a	n/a, 31.77
ST, T6-CRSS$_g$ (MPa)	1.20, 7.47	10.65, 15.86	13.48, n/a	n/a, 9.96
CRSS$_f$ (MPa)	1	1	2	n/a
T5, T6-CRSS$_p$ (MPa)	42	33	60	n/a
T5-CRSS $_1$ (MPa)	55.63, 75.63	115.96, 132.57	145, n/a	n/a
T6-CRSS $_1$ (MPa)	53, 59.27	92.65, 97.86	115.48, n/a	n/a
ST-CRSS $_1$ (MPa)	11, 17.27	59.65, 64.86	55.48, n/a	n/a
T5-CRSS $_2$ (MPa)	57.83, 69.83	132.96, 143.57	219, n/a	n/a, 104.77
T6-CRSS $_2$ (MPa)	55.2, 53.47	109.65, 108.86	189.48, n/a	n/a, 82.96
ST-CRSS $_2$ (MPa)	13.2, 11.47	76.65, 75.86	129.48, n/a	n/a, 86.76
T5-CRSS $_3$ (MPa)	61.83, 72.83	179.96, 188.57	281, n/a	n/a, 111.77
T6-CRSS $_3$ (MPa)	59.2, 56.47	156.65, 153.86	251.48, n/a	n/a, 89.96
ST-CRSS $_3$ (MPa)	17.2, 14.47	123.65, 120.86	191.48, n/a	n/a, 89.96
T6-CRSS $_{PLATT}$ (MPa)	35	75.8	116.7	55.4
T5-CRSS $_*$(MPa)	76	163.2	187.4	116.4
T6-CRSS $_{**}$ (MPa)	47.6	92.2	117.3	84.4
ST-CRSS $_a$	31.37	106.89	97.88	n/a
ST-CRSS $_b$	5.6	59.2	57.3	n/a

Table 9
Optimization bounds provided for calibration of initial slip resistance and corresponding hardening parameters for slip and twining modes of WE43-ST Mg alloy.

Mode	s_0^α (MPa)	h_0^α (MPa)	s_s^α (Mpa)	a^α
Basal	5–32	100–1000	5–500	1–3
Prismatic	59–107	100–1000	59–500	1–3
Pyramidal<a>	59–107	100–1000	59–500	1–3
Pyramidal<c+a>	57–98	100–1000	57–500	1–3
Twinning<c+a>	20–90	100–1000	20–500	1–3

next active slip mode. Twinning and pyramidal $< a >$ are slightly active in the case of the T6 condition sample during tension loading. The twinning mechanism becomes important during compression. Fig. 22 (b) shows that there is more twinning activity in T5 compared to T6. Similar to uniaxial tension, pyramidal $< a >$ slip mode is very important in the T5 condition, while it is only slightly active in the case of T6 condition, which has considerable prismatic slip activity. The results show that the different heat treatment conditions of T5 and T6 exhibit different relative slip activity patterns, which can be attributed to the effect of grain size on the CRSS of each deformation mechanism. For example, in the case of prismatic and pyramidal $< a >$ slip modes, in the case of the T5 condition, $CRSS_{prismatic}/CRSS_{pyramidal<a>} = 1.02$ (see Table 6) while in the case of the T6 condition, $CRSS_{prismatic}/CRSS_{pyramidal<a>} = 0.88$ (see Table 3). Accordingly, the predicted pyramidal $< a >$ is more active than prismatic in the case of the fine-grained T5 condition, while it is almost inactive in the case of the coarse-grained T6 condition.

Table 10

The calibrated values of initial slip resistance and corresponding hardening parameters for slip and twining modes of WE43-ST Mg alloy.

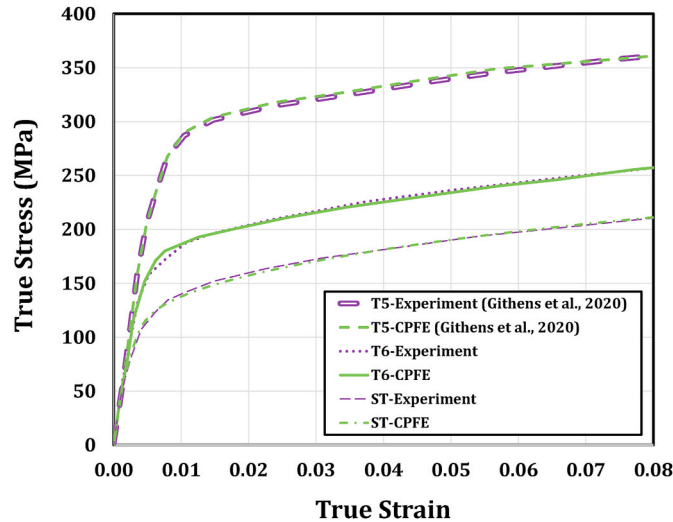| Mode	s_0^α (MPa)	h_0^α (MPa)	s_s^α (Mpa)	a^α
Basal	22	995	80	2.5
Prismatic	72	812	160	2.5
Pyramidal$<a>$	74	773	180	2.5
Pyramidal$<c+a>$	77	721	190	2.5
Twinning$<c+a>$	68	839	120	2.5

Fig. 21. The responses of WE43 Mg alloy samples under ST, T5, and T6 heat treatment conditions during uniaxial tension along RD. The CPFE simulation was compared to the experimental results. The WE43 T5 condition data was reported by Githens et al. (2020).

Table 11

The Hall-Petch constant K (MPa × mm$^{1/2}$) for different slip systems using the CPFE calibrated values of T5 and T6. The values reported by Raeisinia et al. (2011) and Wang and Choo (2014) are also presented.

Mode	CPFE simulation	Wang and Choo (2014)	Raeisinia et al. (2011)
Basal	4.53	2.61	0.42
Prismatic	11.33	5.54	3.72
Pyramidal$<a>$	8.9	n/a	n/a
Pyramidal$<c+a>$	11.18	n/a	4.71
Twinning$<c+a>$	5.1	3.48	n/a

5. Summary and conclusions

An integrated framework was developed using both SEM-DIC experiment and CPFE simulation to investigate the effects of heat treatment on the deformation mechanisms of WE43 Mg. The effects of various heat treatments on macroscopic mechanical properties, including yield strength, ultimate strength, and ductility, were experimentally investigated. In the next step, the deformation mechanisms and response of WE43-T6 were then investigated using crystal plasticity finite element (CPFE) simulation. In the case of WE43-T6, the SEM-DIC results were compared with those obtained using CPFE simulation. Comparisons were made between the displacement and strain fields, and the effect of nominal basal Schmid factor, grain size, and boundary conditions were examined. Finally, the response of the T6 condition was compared to the T5 condition in order to investigate the governing mechanisms of heat treatment effects. The main conclusions can be summarized as follows:

- As-received WE43-T5 samples had a higher yield strength, ultimate strength, and ductility under uniaxial tension as compared to the solution treated and further aged samples. This can be attributed to grain coarsening produced during the solution treatment. The as-received WE43-T5 samples had a smaller average grain size, which led to a higher strength, according to the Hall-Petch model and higher ductility.
- In the case of the solution treated samples and further aged samples, the T6 condition exhibited a higher yield strength and ultimate strength, which is governed by the role of precipitates.
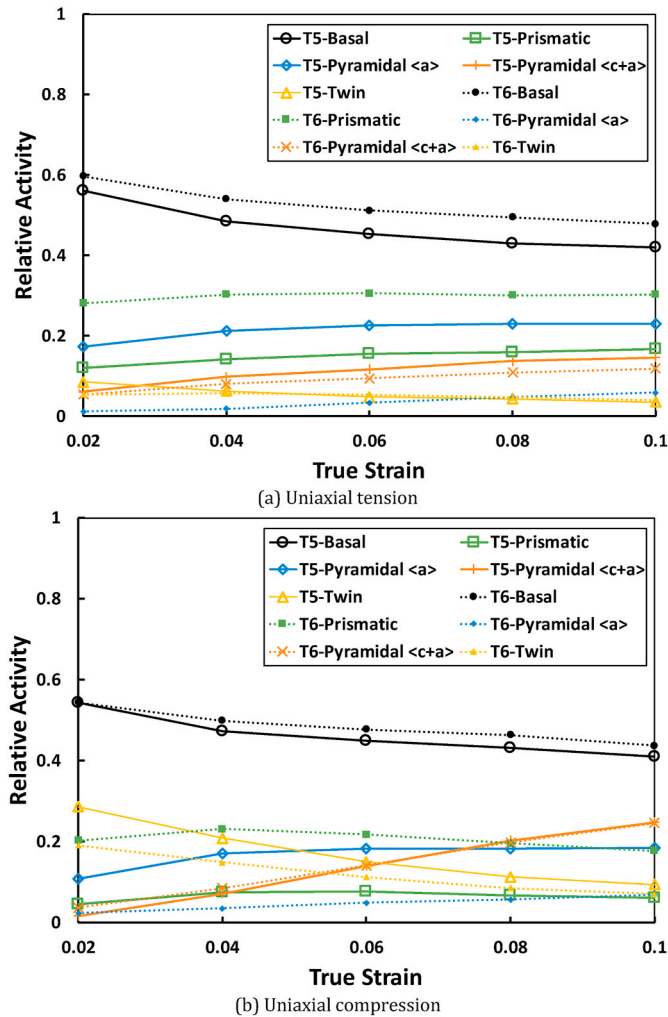
Fig. 22. Predicted relative slip and twinning activities of WE-43 Mg alloy samples under two different heat treatments conditions of T5 and T6 during uniaxial loading along RD: (a) Uniaxial tension (b) Uniaxial compression. The T5 condition data was reported by Githens et al. (2020).

- The CPFE can successfully capture the displacement maps observed in the experiment. Although a few strain localizations are smeared, CPFE provides a good reproduction of the average strains in several grains, with the best matches seen in large grains.
- After the solution heat treatment (ST condition), the precipitates density and size increase with the aging time, which was also reported by Bhattacharyya et al. (2017). However, the grain size does not considerably vary with the aging time. Accordingly, the differences between the responses of underaged samples and the T6 sample can be attributed to precipitate strengthening.
- The CRSS in T5 condition is higher than that of the T6 condition, which can be mainly attributed to the finer grain size of the T5 condition.
- For WE43 Mg, the classic macro-Hall-Petch relationship with a single constant should be modified to capture the observed grain size effects. Accordingly, each deformation mode has a unique Hall-Petch constant, which is in line with the results reported by Raeisinia and Agnew (2010), Raeisinia et al. (2011), Wang and Choo (2014), and Bhattacharyya et al. (2016) for Mg alloys.
- The different heat treatment conditions of T5 and T6 exhibit different relative slip activity patterns, which can be attributed to the effect of grain size on the CRSS of each deformation mechanism. The pyramidal $<a>$ is more active than prismatic in the case of T5 condition, while it is almost inactive in the case of T6 condition.
- In order to further investigate the twinning in WE43 Mg alloy, the experimental information on twin morphology and volume should be provided. Accordingly, a physically based twinning model can enhance the accuracy of the crystal plasticity simulations. Both of these aspects can be developed in the future, which would lead to a better understanding of twinning in WE43 alloys.

Credit Author Statement

Sriram Ganesan: Developing the code; Conceptualization; Formal analysis; Investigation; Methodology; Validation; Visualization;

Writing – original draft; Writing – review & editing. Mohammadreza Yaghoobi: Conceptualization; Formal analysis; Investigation; Methodology; Supervision; Validation; Visualization; Writing – original draft; Writing – review & editing. Alan Githens: Experiments; Conceptualization; Formal analysis; Investigation; Methodology; Validation; Visualization; Writing – original draft; Zhe Chen: Experiments; Formal analysis; Investigation; Validation; Visualization; Samantha Daly: Conceptualization; Project administration; Formal analysis; Investigation; Methodology; Supervision; Writing – review & editing. John E. Allison: Conceptualization; Project administration; Methodology; Funding acquisition; Supervision; Writing – review & editing. Veera Sundararaghavan: Conceptualization; Project administration; Formal analysis; Investigation; Methodology; Supervision; Writing – review & editing

Declaration of competing interest

The authors declare that they have no known competing financial interests or personal relationships that could have appeared to influence the work reported in this paper.

Acknowledgements

Appendix A. Supplementary data

Supplementary data to this article can be found online at https://doi.org/10.1016/j.ijplas.2020.102917.

Appendix A

- PRISMS-Plasticity is an open-source computer code distributed under the GNU Lesser General Public License version 2.1. The source code for PRISMS-Plasticity is available at the following link: https://github.com/prisms-center/plasticity.
- The experimental data and PRISMS-Plasticity input files are available on Materials Commons https://materialscommons.org/and can be found at https://doi.org/10.13011/m3-07fa-gd12.

References

Aagesen, L.K., Adams, J.F., Allison, J.E., et al., 2018. PRISMS: an integrated, open-source framework for accelerating predictive structural materials science. JOM (J. Occup. Med.) 70, 2298–2314.

Abdolvand, H., Daymond, M.R., Mareau, C., 2011. Incorporation of twinning into a crystal plasticity finite element model: evolution of lattice strains and texture in Zircaloy-2. Int. J. Plast. 27, 1721–1738.

Abdolvand, H., Majkut, M., Oddershede, J., Schmidt, S., Lienert, U., Diak, B.J., Withers, P.J., Daymond, M.R., 2015. On the deformation twinning of Mg AZ31B: a three-dimensional synchrotron X-ray diffraction experiment and crystal plasticity finite element model. Int. J. Plast. 70, 77–97.

Adams, J.F., Allison, J.E., Jones, J.W., 2016. The effects of heat treatment on very high cycle fatigue behavior in hot-rolled WE43 magnesium. Int. J. Fatig. 93, 372–386.

Agnew, S.R., Mulay, R.P., Polesak, F.J., Calhoun, C.A., Bhattacharyya, J.J., Clausen, B., 2013. In situ neutron diffraction and polycrystal plasticity modeling of a Mg-Y-Nd-Zr alloy: effects of precipitation on individual deformation mechanisms. Acta Mater. 61, 3769–3780.

Anand, L., Kothari, M., 1996. A computational procedure for rate-independent crystal plasticity. J. Mech. Phys. Solid. 44, 525–558.

Ardeljan, M., McCabe, R.J., Beyerlein, I.J., Knezevic, M., 2015. Explicit incorporation of deformation twins into crystal plasticity finite element models. Comput. Methods Appl. Mech. Eng. 295, 396–413.

Barrett, C.D., El Kadiri, H., 2014. The roles of grain boundary dislocations and disclinations in the nucleation of {1 0 1 2} twinning. Acta Mater. 63, 1–15.

Begum, S., Chen, D.L., Xu, S., Luo, A.A., 2009. Low cycle fatigue properties of an extruded AZ31 magnesium alloy. Int. J. Fatig. 31, 726–735.

Beyerlein, I.J., Arul Kumar, M., 2018. The stochastic nature of deformation twinning: application to HCP materials. In: Andreoni, W., Yip, S. (Eds.), Handbook of M5aterials Modeling : Methods: Theory and Modeling. Springer International Publishing, Cham, pp. 1–39.

Beyerlein, I.J., Capolungo, L., Marshall, P.E., McCabe, R.J., Tome, C.N., 2010. Statistical analyses of deformation twinning in magnesium. Phil. Mag. 90, 2161–2190.

Beyerlein, I.J., McCabe, R.J., Tomé, C.N., 2011. Effect of microstructure on the nucleation of deformation twins in polycrystalline high-purity magnesium: a multi-scale modeling study. J. Mech. Phys. Solid. 59, 988–1003.

Beyerlein, I.J., Tomé, C.N., 2010. A probabilistic twin nucleation model for HCP polycrystalline metals. Proc. Math. Phys. Eng. Sci. 466, 2517–2544.

Bhattacharyya, J.J., Wang, F., Wu, P.D., Whittington, W.R., El Kadiri, H., Agnew, S.R., 2016. Demonstration of alloying, thermal activation, and latent hardening effects on quasi-static and dynamic polycrystal plasticity of Mg alloy, WE43-T5, plate. Int. J. Plast. 81, 123–151.

Bhattacharyya, J.J., Wang, F., McQuade, P.J., Agnew, S.R., 2017. Deformation and fracture behavior of Mg alloy, WE43, after various aging heat treatments. Mater. Sci. Eng., A 705, 79–88.

Capolungo, L., Beyerlein, I.J., 2008. Nucleation and stability of twins in hcp metals. Phys. Rev. B 78, 024117.

Christian, J.W., Mahajan, S., 1995. Deformation twinning. Prog. Mater. Sci. 39, 1–157.

Feather, W.G., Ghorbanpour, S., Savage, D.J., Ardeljan, M., Jahedi, M., McWilliams, B.A., Gupta, N., Xiang, C., Vogel, S.C., Knezevic, M., 2019. Mechanical response, twinning, and texture evolution of WE43 magnesium-rare earth alloy as a function of strain rate: experiments and multi-level crystal plasticity modeling. Int. J. Plast. 120, 180–204.

Fernández, A., Jérusalem, A., Gutiérrez-Urrutia, I., Pérez-Prado, M.T., 2013. Three-dimensional investigation of grain boundary-twin interactions in a Mg AZ31 alloy by electron backscatter diffraction and continuum modeling. Acta Mater. 61, 7679–7692.

Fernández, A., Pérez Prado, M.T., Wei, Y., Jérusalem, A., 2011. Continuum modeling of the response of a Mg alloy AZ31 rolled sheet during uniaxial deformation. Int. J. Plast. 27, 1739–1757.

Ganesan, S., 2017. Microstructural Response of Magnesium Alloys: 3D Crystal Plasticity and Experimental Validation. University of Michigan, Ann Arbor, USA.

Ghorbanpour, S., McWilliams, B.A., Knezevic, M., 2019. Effect of hot working and aging heat treatments on monotonic, cyclic, and fatigue behavior of WE43 magnesium alloy. Mater. Sci. Eng., A 747, 27–41.

Githens, A., Daly, S., 2017. Patterning corrosion-susceptible metallic alloys for digital image correlation in a scanning electron microscope. Strain 53, e12215.

Githens, A., Ganesan, S., Chen, Z., Allison, J., Sundararaghavan, V., Daly, S., 2020. Characterizing microscale deformation mechanisms and macroscopic tensile properties of a high strength magnesium rare-earth alloy: a combined experimental and crystal plasticity approach. Acta Mater. 186, 77–94.

Greeley, D., Yaghoobi, M., Pagan, D., Sundararaghavan, V., Allison, J., 2019. Using synchrotron radiation to improve understanding of deformation of polycrystalline metals by measuring, modelling and publishing 4D information. IOP Conf. Ser. Mater. Sci. Eng. 580, 012017.

Hama, T., Tanaka, Y., Uratani, M., Takuda, H., 2016. Deformation behavior upon two-step loading in a magnesium alloy sheet. Int. J. Plast. 82, 283–304.

Hama, T., Kobuki, A., Takuda, H., 2017. Crystal-plasticity finite-element analysis of anisotropic deformation behavior in a commercially pure titanium Grade 1 sheet. Int. J. Plast. 91, 77–108.

Jahedi, M., McWilliams, B.A., Knezevic, M., 2018. Deformation and fracture mechanisms in WE43 magnesium-rare earth alloy fabricated by direct-chill casting and rolling. Mater. Sci. Eng., A 726, 194–207.

Kabirian, F., Khan, A.S., Gnäupel-Herold, T., 2015. Visco-plastic modeling of mechanical responses and texture evolution in extruded AZ31 magnesium alloy for various loading conditions. Int. J. Plast. 68, 1–20.

Kalidindi, S.R., 1998. Incorporation of deformation twinning in crystal plasticity models. J. Mech. Phys. Solid. 46, 267–271.

Kammers, A.D., Daly, S., 2013. Digital image correlation under scanning electron microscopy: methodology and validation. Exp. Mech. 53, 1743–1761.

Knezevic, M., Levinson, A., Harris, R., Mishra, R.K., Doherty, R.D., Kalidindi, S.R., 2010. Deformation twinning in AZ31: influence on strain hardening and texture evolution. Acta Mater. 58, 6230–6242.

Lentz, M., Klaus, M., Wagner, M., Fahrenson, C., Beyerlein, I.J., Zecevic, M., Reimers, W., Knezevic, M., 2015. Effect of age hardening on the deformation behavior of an Mg–Y–Nd alloy: in-situ X-ray diffraction and crystal plasticity modeling. Mater. Sci. Eng., A 628, 396–409.

Lévesque, J., Mohammadi, M., Mishra, R.K., Inal, K., 2016. An extended Taylor model to simulate localized deformation phenomena in magnesium alloys. Int. J. Plast. 78, 203–222.

Liu, Y., Wei, Y., 2014. A polycrystal based numerical investigation on the temperature dependence of slip resistance and texture evolution in magnesium alloy AZ31B. Int. J. Plast. 55, 80–93.

Lloyd, S., 1982. Least squares quantization in PCM. IEEE Trans. Inf. Theor. 28, 129–137.

Martin, G., Sinclair, C.W., Lebensohn, R.A., 2014. Microscale plastic strain heterogeneity in slip dominated deformation of magnesium alloy containing rare earth. Mater. Sci. Eng., A 603, 37–51.

Mirza, F.A., Chen, D.L., Li, D.J., Zeng, X.Q., 2013. Low cycle fatigue of a rare-earth containing extruded magnesium alloy. Mater. Sci. Eng. 575, 65–73.

Mokdad, F., Chen, D.L., 2015. Strain-controlled low cycle fatigue properties of a rare-earth containing ZEK100 magnesium alloy. Mater. Des. 67, 436–447.

Mukai, T., Yamanoi, M., Watanabe, H., Ishikawa, K., Higashi, K., 2001. Effect of grain refinement on tensile ductility in ZK60 magnesium alloy under dynamic loading. Mater. Trans. 42 (7), 1177–1181.

Murphy-Leonard, A.D., Pagan, D.C., Beaudoin, A., Miller, M.P., Allison, J.E., 2019. Quantification of cyclic twinning-detwinning behavior during low-cycle fatigue of pure magnesium using high energy X-ray diffraction. Int. J. Fatig. 125, 314–323.

Oppedal, A.L., El Kadiri, H., Tomé, C.N., Kaschner, G.C., Vogel, S.C., Baird, J.C., Horstemeyer, M.F., 2012. Effect of dislocation transmutation on modeling hardening mechanisms by twinning in magnesium. Int. J. Plast. 30–31, 41–61.

Oppedal, A.L., El Kadiri, H., Tomé, C.N., Vogel, S.C., Horstemeyer, M.F., 2013. Anisotropy in hexagonal close-packed structures: improvements to crystal plasticity approaches applied to magnesium alloy. Phil. Mag. 93, 4311–4330.

Platts, A.T., 2019. Understanding and Simulating High Strain Rate Deformation of Magnesium WE43 Plate Products. The University of Manchester, United Kingdom).

Prasad, N.S., Narasimhan, R., Suwas, S., 2017. Effects of lattice orientation and crack tip constraint on ductile fracture initiation in Mg single crystals. Int. J. Plast. 97, 222–245.

Qiao, H., Agnew, S.R., Wu, P.D., 2015. Modeling twinning and detwinning behavior of Mg alloy ZK60A during monotonic and cyclic loading. Int. J. Plast. 65, 61–84.

Qiao, H., Barnett, M.R., Wu, P.D., 2016. Modeling of twin formation, propagation and growth in a Mg single crystal based on crystal plasticity finite element method. Int. J. Plast. 86, 70–92.

Quey, R., Dawson, P.R., Barbe, F., 2011. Large-scale 3D random polycrystals for the finite element method: generation, meshing and remeshing. Comput. Methods Appl. Mech. Eng. 200, 1729–1745.

Raeisinia, B., Agnew, S.R., 2010. Using polycrystal plasticity modeling to determine the effects of grain size and solid solution additions on individual deformation mechanisms in cast Mg alloys. Scripta Mater. 63, 731–736.

Raeisinia, B., Agnew, S.R., Akhtar, A., 2011. Incorporation of solid solution alloying effects into polycrystal modeling of Mg alloys. Metall. Mater. Trans. 42A, 1418–1430.

Sedighiani, K., Diehl, M., Traka, K., Roters, F., Sietsma, J., Raabe, D., 2020. An efficient and robust approach to determine material parameters of crystal plasticity constitutive laws from macro-scale stress–strain curves. Int. J. Plast. 134, 102779.

Shade, P.A., Musinski, W.D., Obstalecki, M., Pagan, D.C., Beaudoin, A., Bernier, J.V., Turner, T.J., 2019. Exploring new links between crystal plasticity models and high-energy X-ray diffraction microscopy. Curr. Opin. Solid State Mater. Sci. 23, 100763.

Shi, B.Q., Chen, R.S., Ke, W., 2013. Influence of grain size on the tensile ductility and deformation modes of rolled Mg–1.02 wt.% Zn alloy. Journal Magnesium & Alloys 1, 210–216.

Sitzmann, E., Marquis, E.A., 2015. Chemistry and morphology of β′ precipitates in an aged Mg-Nd-Y-Zr alloy. Phil. Mag. Lett. 95, 7–13.

Staroselsky, A., Anand, L., 2003. A constitutive model for hcp materials deforming by slip and twinning: Application to magnesium alloy AZ31B. Int. J. Plast. 19, 1843–1864.

Stanford, N., Cottam, R., Davis, B., Robson, J., 2014. Evaluating the effect of yttrium as a solute strengthener in magnesium using in situ neutron diffraction. Acta Mater. 78, 1–13.

Sutton, M.A., Li, N., Garcia, D., Cornille, N., Orteu, J.-J., McNeill, S.R., Schreier, H.W., Li, X., Reynolds, A.P., 2007a. Scanning electron microscopy for quantitative small and large deformation measurements part II: experimental validation for magnifications from 200 to 10,000. Exp. Mech. 47, 789–804.

Sutton, M.A., Li, N., Garcia, D., Cornille, N., Orteu, J.J., McNeill, S.R., Schreier, H.W., Li, X., 2006. Metrology in a scanning electron microscope: theoretical developments and experimental validation. Meas. Sci. Technol. 17, 2613.

Sutton, M.A., Li, N., Joy, D.C., Reynolds, A.P., Li, X., 2007b. Scanning electron microscopy for quantitative small and large deformation measurements part I: SEM imaging at magnifications from 200 to 10,000. Exp. Mech. 47, 775–787.

Tomé, C.N., Lebensohn, R.A., Kocks, U.F., 1991. A model for texture development dominated by deformation twinning: Application to zirconium alloys. Acta Metall. Mater. 39, 2667–2680.

Van Houtte, P., 1978. Simulation of the rolling and shear texture of brass by the Taylor theory adapted for mechanical twinning. Acta Metall. 26, 591–604.

Voyiadjis, G.Z., Yaghoobi, M., 2019a. Chapter 1 - introduction: size effects in materials. In: Voyiadjis, G.Z., Yaghoobi, M. (Eds.), Size Effects in Plasticity. Academic Press, pp. 1–79.

Voyiadjis, G.Z., Yaghoobi, M., 2019b. Chapter 3 - nonlocal crystal plasticity. In: Voyiadjis, G.Z., Yaghoobi, M. (Eds.), Size Effects in Plasticity. Academic Press, pp. 191–232.

Wang, J., Hirth, J.P., Tomé, C.N., 2009. $(1\bar{1}012)$ Twinning nucleation mechanisms in hexagonal-close-packed crystals. Acta Mater. 57, 5521–5530.

Wang, H., Wu, P.D., Wang, J., 2013a. Modeling inelastic behavior of magnesium alloys during cyclic loading-unloading. Int. J. Plast. 47, 49–64.

Wang, H., Wu, P.D., Wang, J., Tomé, C.N., 2013b. A crystal plasticity model for hexagonal close packed (HCP) crystals including twinning and de-twinning mechanisms. Int. J. Plast. 49, 36–52.

Wang, L., Huang, Z., Wang, H., Maldar, A., Yi, S., Park, J.-S., Kenesei, P., Lilleodden, E., Zeng, X., 2018. Study of slip activity in a Mg-Y alloy by in situ high energy X-ray diffraction microscopy and elastic viscoplastic self-consistent modeling. Acta Mater. 155, 138–152.

Wang, Y., Choo, H., 2014. Influence of texture on Hall–Petch relationships in an Mg alloy. Acta Mater. 81, 83–97.

Wu, L., Agnew, S.R., Ren, Y., Brown, D.W., Clausen, B., Stoica, G.M., Wenk, H.R., Liaw, P.K., 2010. The effects of texture and extension twinning on the low-cycle fatigue behavior of a rolled magnesium alloy. AZ31B. Materials Science and Engineering A 527, 7057–7067.

Xiang, C., Gupta, N., Coelho, P., Cho, K., 2018. Effect of microstructure on tensile and compressive behavior of WE43 alloy in as cast and heat treated conditions. Mater. Sci. Eng., A 710, 74–85.

Yaghoobi, M., Allison, J.E., Sundararaghavan, V., 2020. Multiscale modeling of twinning and detwinning behavior of HCP polycrystals. Int. J. Plast. 102653.

Yaghoobi, M., Ganesan, S., Sundar, S., Lakshmanan, A., Rudraraju, S., Allison, J.E., Sundararaghavan, V., 2019. PRISMS-Plasticity: an open-source crystal plasticity finite element software. Comput. Mater. Sci. 169, 109078.

Yu, K., Li, W., Wang, R., Wang, B., Li, C., 2008. Effect of T5 and T6 tempers on a hot-rolled WE43 magnesium alloy. Mater. Trans. 49, 1818–1821.

Yu, Q., Jiang, Y., Wang, J., 2015. Cyclic deformation and fatigue damage in single-crystal magnesium under fully reversed strain-controlled tension-compression in the [1010] direction. Scripta Mater. 96, 41–44.

Zhang, J., Joshi, S.P., 2012. Phenomenological crystal plasticity modeling and detailed micromechanical investigations of pure magnesium. J. Mech. Phys. Solid. 60, 945–972.

Zheng, S.J., Beyerlein, I.J., Wang, J., Carpenter, J.S., Han, W.Z., Mara, N.A., 2012. Deformation twinning mechanisms from bimetal interfaces as revealed by in situ straining in the TEM. Acta Mater. 60, 5858–5866.